

Department of Physics and Astronomy
Heidelberg University

Bachelor Thesis in Physics

submitted by

Johann Nicolas Himbert

born in Saarbrücken (Germany)

October 2023

Towards a Measurement of CP Asymmetry in $D_{(s)}^{\pm} \rightarrow K^{\pm}\eta'$

This Bachelor Thesis has been carried out by Johann Nicolas Himbert at the
Physikalisches Institut in Heidelberg
under the supervision of
Prof. Stephanie Hansmann-Menzemer

Abstract

The first steps towards a CP asymmetry measurement in $D_{(s)}^+ \rightarrow \eta' K^+$ decays is performed using 5.7 fb^{-1} data of Run2 of the LHCb experiment at a centre-of-mass energy of 13 TeV. A statistical uncertainty of

$$\sigma_{stat}(A_{CP}(D^+ \rightarrow \eta' K^+)) = 1.9\% \text{ and}$$

$$\sigma_{stat}(A_{CP}(D_s^+ \rightarrow \eta' K^+)) = 0.7\%$$

is evaluated, by reconstructing $\eta' \rightarrow \pi^+ \pi^- \gamma$ with a total number of $N(D^+ \rightarrow \eta' K^+) = 13890 \pm 266$ and $N(D_s^+ \rightarrow \eta' K^+) = 51342 \pm 352$ reconstructed events. Thus the measurement of CP asymmetries on this data set results in the best to date and the first for the decay $D^+ \rightarrow \eta' K^+$.

Kurzfassung

Diese Bachelorarbeit legt den Grundstein für eine spätere Analyse der CP Asymmetrie in den beiden Zerfällen $D_{(s)}^+ \rightarrow \eta' K^+$. Dabei werden 5.7 fb^{-1} an Daten vom Run2 des LHCb Detektors bei einer Schwerpunktsenergie von 13 TeV verwendet. Das neutrale η' wird über den Zerfall $\eta' \rightarrow \pi^+ \pi^- \gamma$ rekonstruiert und eine Gesamtanzahl der Ereignisse von $N(D^+ \rightarrow \eta' K^+) = 13890 \pm 266$ und $N(D_s^+ \rightarrow \eta' K^+) = 51342 \pm 352$ ist das Resultat dieser Analyse. Daraus folgt ein statistischer Fehler für die CP Asymmetrie in den beiden Zerfällen von

$$\sigma_{stat}(A_{CP}(D^+ \rightarrow \eta' K^+)) = 1.9\% \text{ und}$$

$$\sigma_{stat}(A_{CP}(D_s^+ \rightarrow \eta' K^+)) = 0.7\%.$$

Diese Messung der CP Asymmetrie ist die bisher beste und die erste für den Zerfall $D^+ \rightarrow \eta' K^+$.

Table of Contents

List of abbreviations.....	vi
1 Introduction.....	1
2 Theoretical framework.....	2
2.1 The Standard Model.....	2
2.2 CP asymmetries in charm decays.....	3
2.2.1 CP violation.....	3
2.2.2 The CKM matrix.....	4
2.2.3 Charmed meson.....	5
2.3 The $D(s)\pm \rightarrow \eta' K \pm$ channels.....	6
3 The LHCb experiment.....	8
3.1 LHC.....	8
3.2 The LHCb-detector.....	9
3.2.1 The Vertex locator.....	10
3.2.2 The magnet.....	11
3.2.3 The Tracker Turicensis.....	11
3.2.4 The inner and outer tracker.....	11
3.2.5 The particle identification.....	12
3.3 The trigger system.....	13
4 Monte-Carlo simulation.....	13
5 Measuring direct CP asymmetries.....	14
6 Data set and trigger selection.....	17
6.1 The trigger.....	17
6.1.1 The trigger selection.....	18
7 General overview of the analysis.....	20
8 Secondary decays.....	21
8.1 Selection for a cut on the impact parameter.....	21
8.2 Estimate on the impact of secondary decays to the systematic uncertainty.....	24
9 MVA classifier.....	25
9.1 BDT classifier.....	25
9.2 Offline selection.....	27
9.3 Input variables of the BDT.....	29
9.3 Training samples.....	31
9.4 BDT parameter scan.....	32
9.5 Cut on the output of the BDT.....	34
10 Background analysis.....	40
10.1 Comparing background decays.....	42

10.2 Technique to remove background decays	45
11 Fit routine	47
12 Conclusion.....	49
Appendix	I
A Trigger lines.....	I
B Offline selection cuts on $m(\pi + \pi^-)$ and $m(\pi + \pi - K)$.....	II
C $m(\eta')$ fit	IV
D BDT Analysis.....	V
E Scan for best BDT parameters.....	VIII
F Determine the BDT cut	X
G Fit parameter	XIII
Bibliography	XIV
Acknowledgement	XVI

List of abbreviations

In this section important physical quantities are defined.

DTF: The decay tree fitter (DTF) [1] takes the complete decay chain into account and parameterizes it as function of the vertex positions, decay lengths and momenta. Then, these parameters are fitted simultaneously and additionally constraints such as masses of particles or 4-momentum conservation at each vertex are taken into account.

PV: The primary vertex is the point in space, where the first interaction between two protons from the beam happens.

$m(D)_{DTF}^{\eta'}$: Mass of D meson, which is calculated with the DTF and a constrain on the η' mass. For simplicity, it is referred to as $m(D)_{DTF}$ in this thesis.

OWNPV: Origin vertex with respect to the particle.

ENDVERTEX: Position of the reconstructed decay vertex of the particle.

IP: Impact parameter is the perpendicular distance between the reconstructed track and its PV.

χ_{IP}^2 : Difference in the χ^2 of the PV fit with and without considering the particles of the decay.

ndof: Number of degrees of freedom. It can be determined by subtracting the number of floating parameters from the number of data points.

p: Momentum of a particle .

p_T : Momentum of a particle transverse to the beam line.

FD: Flight distance between the origin vertex and the decay vertex of the particle.

γ_{CL} : It is used for the identification of photons and their separation from hadrons. It takes into account information from the SPD/PS system as well as the shower shape and energy distribution of ECAL clusters [2].

$\gamma_{ISPhoton}$: It's a multivariate analysis tool used to separate π^0 's from photons. It takes into account the cluster size and shape to decide whether it is a good photon candidate [3].

Θ_{Dira} : Direction angle between the momentum of the particle and the vector between the PV and the decay vertex.

P_{Ghost} : Probability that the track is a misreconstructed "fake" track ("ghost track").

η : The pseudorapidity is correlated to the momentum of the particles

$$\eta = \frac{1}{2} * \log \left(\frac{|\vec{p}| + p_L}{|\vec{p}| - p_L} \right) = \operatorname{arctanh} \left(\frac{p_L}{|\vec{p}|} \right).$$

χ_{trk}^2 : χ^2 of the track fit.

$DLL_{K\pi}$: Difference of log-likelihood between the kaon and the pion hypothesis from the PID information:

$$\Delta \log(L_{K\pi}) = \log(L_K) - \log(L_\pi) = \log \left(\frac{L_K}{L_\pi} \right).$$

The higher the DLL value is, the more favoured the kaon hypothesis is compared to the pion hypothesis. In this thesis, a similar quantity, the $PIDx \equiv DLL_{x\pi}$, will be used, where x can be any particle. To compare two particle hypothesis x and y, one can use the relation:

$$DLL_{xy} = DLL_{x\pi} - DLL_{y\pi} = \log \left(\frac{L_x}{L_y} \right).$$

For higher values of DLL_{xy} , the x hypothesis is the favoured one [4].

1 Introduction

The Standard Model (SM) of particle physics is at the moment the best theoretical model to describe fundamental interactions. It has demonstrated huge success providing a very large number of precise predictions that were confirmed by numerous experiments. However, it fails to explain some open questions like the baryon asymmetry [5], dark matter or how to include the gravitational force into the model. This leads to a wide search for physics Beyond the Standard Model (BSM) by looking at allowed physical processes and search for a deviation from the theoretical predictions or by directly search for e.g. dark matter candidates.

One of the most important fields is the study of CPV (violation of symmetry under charge parity transformation). CP violation is very sensitive to interference with loop diagrams and therefore is an excellent tool for direct searches for BSM phenomena. There are a lot of possible sectors where one can study CPV. The D sector is of interest, because D mesons include a charm quark, which is the heaviest up-type quark that can be studied with large statistics at the LHCb. The first CPV in the charm sector was established in 2019 by the LHCb collaboration [6]. This milestone has triggered further investigations in the charm sector and has proven the ability to perform direct CP asymmetry (A_{CP}) measurements.

This thesis studies the decay channels $D_{(s)}^+ \rightarrow \eta' K^+$, where the η' meson is reconstructed in the $\pi^+ \pi^- \gamma$ final state, using data collected during Run2 of the LHCb experiment at a centre-of-mass energy of $\sqrt{s} = 13$ TeV and an integrated luminosity of 5.7 fb^{-1} . This thesis optimizes the selection and evaluates the sensitivity for a future CP asymmetry measurement in these channels.

Previously, there was a measurement of $A_{CP}(D_s^+ \rightarrow \eta' K^+) = 0.06 \pm 0.19$ in 2010 from the CLEO collaboration using $\eta' \rightarrow e^+ e^-$ with an integrated luminosity of $L_{int} = 586 \text{ pb}^{-1}$ and a centre-of-mass energy of $\sqrt{s} = 4170$ MeV [7]. For the double Cabibbo suppressed mode $D^+ \rightarrow K^+ \eta'$ there is, so far, no measurement. This thesis establishes that the measurement of CP asymmetries on the studied data set will supersede previous analysis. The theoretical prediction for the D_s^+ channel is $A_{theo}^{CP}(D_s^+ \rightarrow \eta' K^+) = -0.41 * 10^{-3}$ [8].

2 Theoretical framework

This section gives a brief overview of the Standard Model in general and of the CP asymmetry in charmed decays in particular.

2.1 The Standard Model

The SM describes the known elementary particles and the interaction between them. It consist of four different particle types: quarks, leptons, gauge bosons and the Higgs boson (see Figure 1). A subclass of these particles are the fermions. They have spin $\frac{1}{2}$ and are divided into quarks and leptons. Fermions are further subdivided into three different generations. The gauge bosons have spin 1 and are the mediators for the three fundamental interactions: electromagnetic-, strong- and weak interaction.

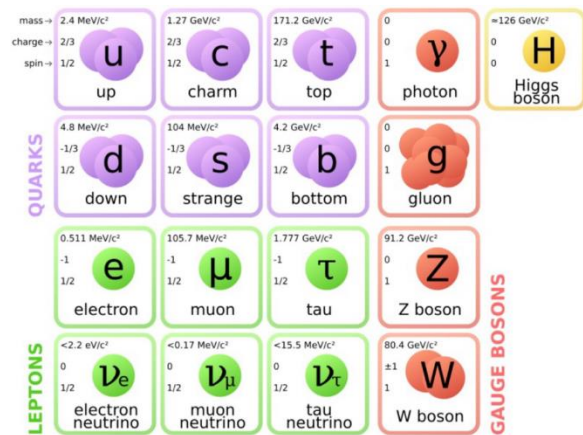


Figure 1: Standard Modell [9].

The mediator of the electromagnetic interaction is the photon. All particles with charge [all besides the neutrinos, the Z^0 and the Higgs boson] couple to the photon and the coupling strength is proportional to the fine structure constant $\alpha \approx \frac{1}{137}$. The potential for this interaction is the coulomb potential which has the form $\sim \frac{1}{r}$. Thus, the electromagnetic interaction decreases with increasing distance between two charged particles.

The strong interaction acts on particles that carry a colour charge, which are quarks and gluons. The potential for this interaction is given by $V(r) = -\frac{4}{3} * \frac{\alpha_s * \hbar * c}{2 * \pi * r} + k * r$ and rises at larger distances between two quarks. This is the reason quarks are not found as free particles but are confined in bound states. These states are called hadrons and are divided into mesons and baryons. Mesons consist of a quark and an antiquark and are colour neutral. Baryons consist of three quarks (antiquarks) and have to be colour neutral too, which means that the quarks in this state must have the colours red, green, and blue (antired, antigreen, antiblue). The

mediators for this interaction are the gluons with a corresponding coupling constant of $\alpha_s \sim 1$. The gluons themselves have a colour charge. There exist in total eight different gluons.

The weak interaction couples to all particles in the SM since all of them carry weak charge. The mediators, which are called W^\pm and Z^0 bosons, have, in contrary to the other gauge bosons, a non-zero mass. The coupling constant for the weak interaction is $\alpha_w \sim \frac{1}{30}$ and is thus greater than the one from the electromagnetic interaction, but the heavy masses of the gauge bosons ($m(W^\pm) = (80.377 \pm 0.012) \text{ GeV}/c^2$, $m(Z^0) = (91.1876 \pm 0.0021) \text{ GeV}/c^2$) [10] lead to a weaker coupling. [11]

The Higgs boson was the last missing particle of the SM discovered in 2012 by the ATLAS and CMS collaborations at the LHC and gives bosons their mass. It has a mass of $m(H) = (125.25 \pm 0.17) \text{ GeV}/c^2$ [12].

2.2 CP asymmetries in charm decays

To measure CP asymmetries, one has to understand the underlying theoretical concept. The next section will give a brief overview of the weak interaction and the concept of CP violation.

2.2.1 CP violation

The C and P are short notations for the charge conjugation (C) and spatial parity (P) symmetry transformations. Charge conjugation is defined with the corresponding operator C:

$$\hat{C}: q \rightarrow \bar{q}. \quad (1)$$

This operator inverts all charged quantum numbers.

The P operator inverts all spatial coordinates:

$$\hat{P}: \vec{p} \rightarrow -\vec{p}. \quad (2)$$

The SM is related to quantum field theories, which are invariant under CPT transformation [13]. The T operator is the time reversal operator. CP symmetry is only violated in the weak interaction, but the strong interaction does not predict CPV.

2.2.2 The CKM matrix

The Cabibbo-Kobayashi-Maskawa (CKM) matrix describes the weak interaction between quarks in the SM. It relates the weak eigenstates (d' , s' , b') with the mass eigenstates (d , s , b) by

$$\begin{pmatrix} d' \\ s' \\ b' \end{pmatrix} = \begin{pmatrix} V_{ud} & V_{us} & V_{ub} \\ V_{cd} & V_{cs} & V_{cb} \\ V_{td} & V_{ts} & V_{tb} \end{pmatrix} * \begin{pmatrix} d \\ s \\ b \end{pmatrix}. \quad (3)$$

The CKM-matrix is unitary, so that

$$V_{CKM} * V_{CKM}^T = I_{3 \times 3}. \quad (4)$$

The condition of unity reduces the number of free parameters to four. They can be approximated as three rotation angles ϕ_{12} , ϕ_{23} , ϕ_{13} and a complex phase δ' .

$$V_{CKM} = \begin{pmatrix} V_{ud} & V_{us} & V_{ub} \\ V_{cd} & V_{cs} & V_{cb} \\ V_{td} & V_{ts} & V_{tb} \end{pmatrix} \approx \begin{pmatrix} 1 & 0 & 0 \\ 0 & c_{23} & s_{23} \\ 0 & -s_{23} & c_{23} \end{pmatrix} * \begin{pmatrix} c_{13} & 0 & s_{13}e^{-i\delta'} \\ 0 & 1 & 0 \\ -s_{13}e^{i\delta'} & 0 & c_{13} \end{pmatrix} * \begin{pmatrix} c_{12} & s_{12} & 0 \\ -s_{12} & c_{12} & 0 \\ 0 & 0 & 1 \end{pmatrix}. \quad (5)$$

with a shorthand notation for the rotation angles, where $s_{ij} = \sin(\phi_{ij})$, $c_{ij} = \cos(\phi_{ij})$. If CP violation is present, then the complex phase has to be non zero. The approximation in (5) is for small orders. For higher orders the complex phase is present in the other matrix elements too.

The absolute values of the CKM-matrix elements are

$$\begin{pmatrix} |V_{ud}| & |V_{us}| & |V_{ub}| \\ |V_{cd}| & |V_{cs}| & |V_{cb}| \\ |V_{td}| & |V_{ts}| & |V_{tb}| \end{pmatrix} = \begin{pmatrix} 0.97401 \pm 0.00011 & 0.22650 \pm 0.00048 & 0.00361^{+0.00011}_{-0.00009} \\ 0.22636 \pm 0.00048 & 0.97320 \pm 0.00011 & 0.04053^{+0.00083}_{-0.00061} \\ 0.00854^{+0.00023}_{-0.00016} & 0.03978^{+0.00082}_{-0.00060} & 0.999172^{+0.000024}_{-0.000035} \end{pmatrix}. \quad (6)$$

The transition between quarks is transformed by exchange of W^\pm bosons. This happens only between up- and down-type quarks. The mixing between quarks of the same generation are of the order $O(1)$, transitions between the first and the second generation are of the order $O(10^{-1})$ and between the first and the third generation of the order $O(10^{-3})$ [14].

2.2.3 Charmed meson

CPV is present in the interference of two diagrams, most of the time a tree and a penguin diagram. In tree diagrams only the matrix elements of the upper left corner of the CKM matrix are involved. We can classify the decays of mesons with a charm quark due to the suppression of the CKM matrix:

- Cabibbo favoured (CF) with amplitudes which are proportional to $V_{ud}V_{cs}^*$
- Single Cabibbo suppressed (SCS) with amplitudes which are proportional to $V_{us}V_{cs}^*$ or $V_{ud}V_{cd}^*$
- Double Cabibbo suppressed (DCS) with amplitudes which are proportional to $V_{us}V_{cd}^*$

The decay $D^+ \rightarrow K^+\eta'$ is a DCS channel since the amplitude is proportional to $V_{us}V_{cd}^*$.

The decay $D_s^+ \rightarrow K^+\eta'$ is a SCS decay. The corresponding amplitude is proportional to $V_{us}V_{cs}^*$.

The penguin diagram involves more elements of the CKM matrix.

2.3 The $D_{(s)}^{\pm} \rightarrow \eta' K^{\pm}$ channels

This thesis will discuss the two decay channels: $D^+ \rightarrow \eta' K^+$ and $D_s^+ \rightarrow \eta' K^+$. The $D_{(s)}^{\pm}$ meson has the quark content $c\bar{d}(c\bar{s})$ for the positive charged meson and the corresponding charge conjugated content for the negative charged one. The D^+ meson has a mass of $m(D^+) = 1869.66 \text{ MeV}/c^2$ and a mean lifetime of $\tau(D^+) = 1.033 \text{ ps}$. The D_s^+ meson has a mass of $m(D_s^+) = 1968.35 \text{ MeV}/c^2$ and a mean lifetime of $\tau(D_s^+) = 0.504 \text{ ps}$ [10].

The kaon (K^+) is a meson with a strange quark ($u\bar{s}$) and has a lower mass of $m(K^+) = 493.677 \text{ MeV}/c^2$. With a mean lifetime of $\tau(K^+) = 12.38 \text{ ns}$ it is more stable than the two D mesons [10].

The $\eta'(958)$ ¹ is a neutral meson with a mass of $m(\eta') = 957.78 \text{ MeV}/c^2$ and is a SU(3) flavour singlet, with the quark content: $\frac{1}{\sqrt{6}} * (u\bar{u} + d\bar{d} + s\bar{s})$. Since this meson has a short lifetime of $3.2 * 10^{-21} \text{ s}$, it is reconstructed using the $\eta' \rightarrow \pi^+ \pi^- \gamma$ decay mode. This channel is used due to its large branching ratio (BR) (see Table 1) and because it does not include any neutral hadrons [10].

In Figure 2 and Figure 3 the leading order Feynman diagrams for both decays are displayed.

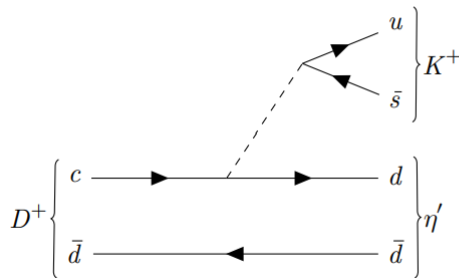


Figure 3: Leading order Feynman diagram for the decay $D^+ \rightarrow \eta' K^+$.

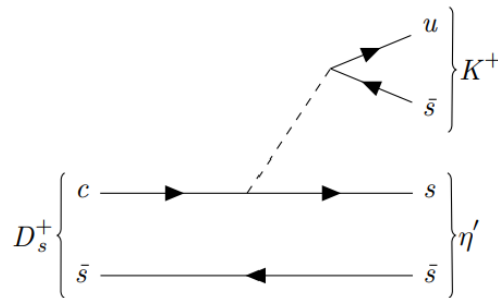


Figure 2: Leading order Feynman diagram for the decay $D_s^+ \rightarrow \eta' K^+$.

A schematic representation of the complete decay chain is shown in Figure 4. Here it can be seen which particles can actually be measured directly in the detector (blue), which particles are intermediate states (orange) and which particles are promptly produced in the proton-proton (pp)-collision (green).

¹ In the thesis it is often referred as η'

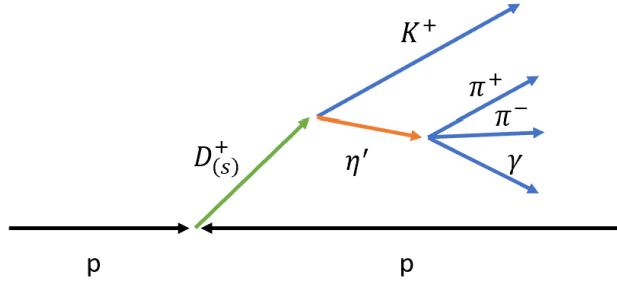


Figure 4: Schematic of the decay.

To get a feeling for the statistics that is needed to analyse the decay one can have a look at the branching ratio of the decays (see Table 2). The detector system of the LHCb experiment is not able to detect the η' directly due to its short lifetime, so the BR of the η' meson has to be taken into account. The product of the two BRs of the $D_{(s)}^+$ and η' is calculated in Table 3.

Table 1: Branching ratios for η' decay channels.

Channel	BR (%)
$\eta' \rightarrow \pi^+ \pi^- \gamma$	29.5 ± 0.4
$\eta' \rightarrow \pi^+ \pi^- \eta$	42.5 ± 0.5
$\eta' \rightarrow \gamma \gamma$	2.307 ± 0.033
$\eta' \rightarrow \pi^0 \pi^0 \eta$	22.4 ± 0.5

Table 2: Branching ratios for the $D_{(s)}^+$ decay channels that are studied in this thesis.

Channel	BR (10^{-3})
$D^+ \rightarrow \eta' K^+$	0.185 ± 0.020
$D_s^+ \rightarrow \eta' K^+$	2.64 ± 0.24

Table 3: Combined branching ratios of Table 2 with the BR of $\eta' \rightarrow \pi^+ \pi^- \gamma$ from Table 1.

Channel	$\Pi(10^{-5})$
$D^+ \rightarrow \eta' K^+, \eta' \rightarrow \pi^+ \pi^- \gamma$	5.4575 ± 0.008
$D_s^+ \rightarrow \eta' K^+, \eta' \rightarrow \pi^+ \pi^- \gamma$	77.88 ± 0.096

3 The LHCb experiment

This section will give an overview of the LHCb experiment with its detector.

3.1 LHC

The Large Hadron Collider (LHC) at CERN (near Geneva) is a collider for protons and heavy ions. It is the world's largest and most powerful accelerator for this purpose. The LHC hosts four large experiments: ATLAS and CMS are general purpose detectors, ALICE specializes in heavy-ion physics and LHCb is designed for flavour physics (see Figure 5).

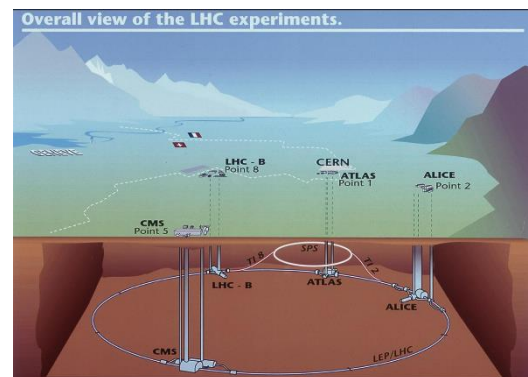


Figure 5: Overview of LHC [15].

The LHC started running in 2011 with a centre-of-mass energy of $\sqrt{s} = 7 - 8$ TeV. After the first long shutdown (LS1) from 2013-2015 the centre-of-mass energy has been increased to $\sqrt{s} = 13$ TeV, which corresponds to a beam energy of 6.5 TeV. In LS2 from 2019-2022 the LHCb detector was upgraded. The goal of this upgrade was to replace the hardware trigger with a new 40 MHz software trigger and to match the requirements due to the higher occupancy from the proposed increased instantaneous luminosity which is a factor of five times larger than the one during Run2. In Run3 the centre-of-mass energy is proposed to reach $\sqrt{s} = 14$ TeV.

This thesis uses data from Run2 of the LHC, so the LHCb detector configuration during Run2 will be discussed in this chapter.

3.2 The LHCb-detector

The LHCb-detector (see Figure 7) is a single arm forward spectrometer with an acceptance of $2 < \eta < 5$, corresponding to $10 < \theta < 250$ (300) mrad in the non-bending (bending) plane. This acceptance is chosen because it is the range where most $b\bar{b}$ -pairs are produced (see Figure 6).

The LHCb is dedicated to study flavour physics and is optimized to study B and D meson decays. One part of the broad physics program consists of the measurement

of CP asymmetries in B and D decay channels as well as branching fractions for rare B decays. With these precise measurements possibly a deviation to the theoretical predictions of the Standard Model can be found which will give a hint for possible BSM physics.

The Tracking system consist of the vertex locator (VELO), the Tracker Turicensis (TT) and the Inner and Outer Tracker (IT/OT). For particle identification, two Ring-Imaging-Cherenkov detectors (RICH), an electromagnetic- and a hadronic calorimeter (ECAL, HCAL) as well as a muon system are used. The LHCb coordinate system is right-handed, with the z axis pointing along the beam axis, y in the vertical direction, and x in the horizontal direction. The (x, z) plane is the bending plane of the dipole magnet.

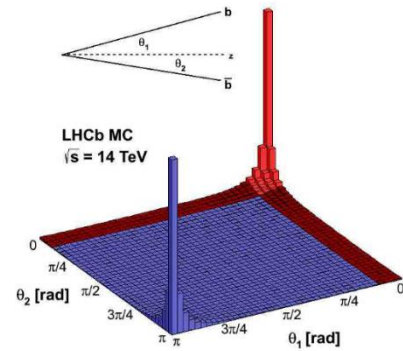


Figure 6: Angular correlation simulation from PYTHIA for $b\bar{b}$ production. Acceptance of the LHCb detector in red [16].

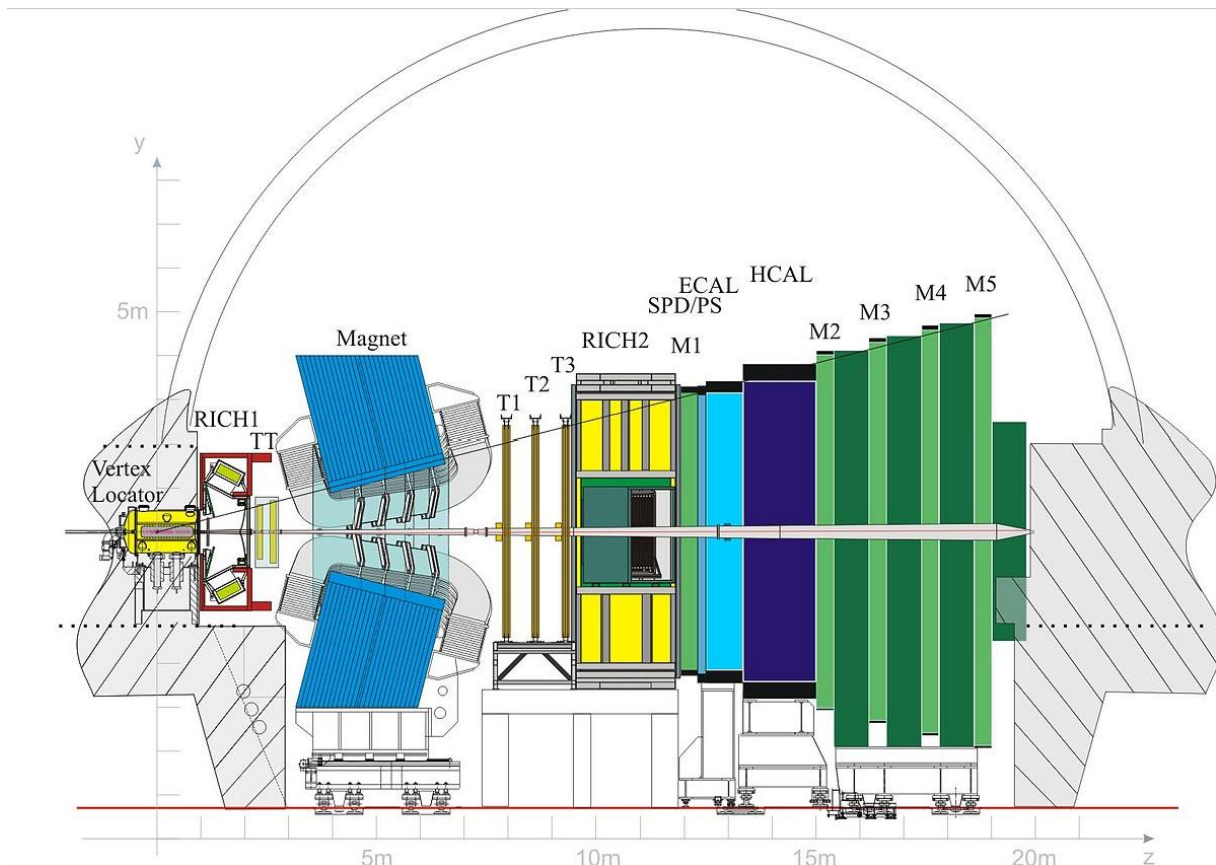


Figure 7: Layout of the LHCb detector for Run2 in the y-z plane [17].

3.2.1 The Vertex locator

The VELO is a 1 m long silicon strip detector for charged particles near the interaction point (IAP). A good track separation is needed, in order to clearly separate secondary from prompt decays. For separating these decays the impact parameter (IP) plays a key role and has to be measured. The IP resolution of $\sigma_{IP} = \left(15 + \frac{29}{p_T [GeV/c]}\right) \mu m$ can be achieved. The VELO uses 41

modules which consists of two semi-circular shapes that can be moved towards the beam. The modules use silicon micro-strip detectors in a r-and ϕ -geometry (see Figure 8). These modules can be moved to a minimum distance of 8.1 mm to the IAP after the LHC beam is stable.

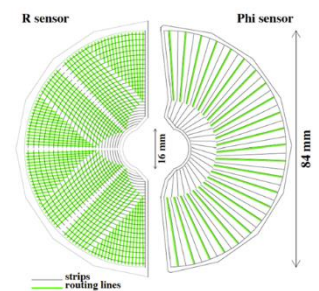


Figure 8: Geometry of the VELO [18].

3.2.2 The magnet

The LHCb experiment uses a dipole magnet with a magnetic field of 4 Tm integrated over 10 m. The saddle-shaped magnets produce a maximum magnetic field of around 1 T in its centre (see Figure 9). Together with the TT and IT/OT it is used to determine the transversal momentum by measuring the deflection angle due to bending of moving charge particles in the presence of a magnetic field. This angle between the incoming and outgoing track after the magnetic field is inverse related to the transverse momentum. To perform the measurement, tracking stations before (TT) and after (IT/OT) the magnet are needed, with a good resolution in x and y direction [20].

At low momenta the resolution of the tracking systems is $\frac{\Delta p}{p} = 0.5\%$ and increases up to 1% at $p = 200 \text{ GeV}/c$.

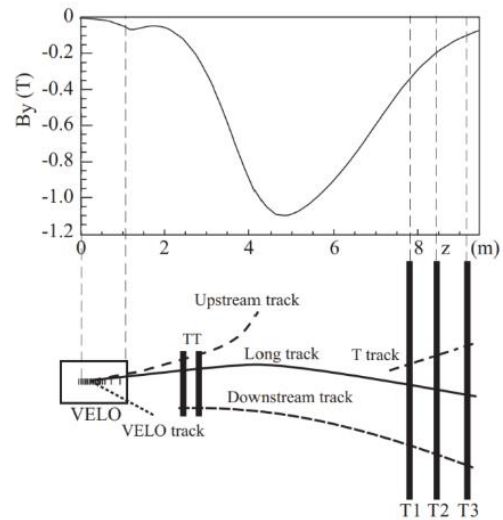


Figure 9: Magnetic field of the LHCb dipole magnet [19].

3.2.3 The Tracker Turicensis

The TT consists of two modules with four layers each and is placed upstream of the magnet. The first and last layer are parallel to the x-y coordinates of the detector (called x layer) and are used for measuring the x component of the transverse momentum. The second and third layer are tilted by an angle of $+5^\circ$ and -5° (u, v layer) to measure the y component. This configuration is used since the detectors are silicon strip detectors and can only measure one coordinate with a resolution of $50 \mu\text{m}$.

3.2.4 The inner and outer tracker

The T-stations (T1-T3) consist of three modules with four layers each and the same (x, u, v, x) configuration as the TT. Inner and Outer Tracker refer here to the location in a layer with respect to the beam pipe. The IT only covers an area of 0.35 m^2 of silicon microstrip detectors

with a resolution of $50 \mu\text{m}$. Despite its small coverage of the T stations around 50% of the tracks go through the IT, because the density of tracks is higher near the beam pipe. The OT consists of gas straw detectors that cover most of the $5 \times 6 \text{ m}^2$, but has a worse resolution of $200 \mu\text{m}$.

3.2.5 The particle identification

The two RICH detectors are used to identify charged particles by measuring the Cherenkov angle, which depends on the particle mass and the momentum (see Figure 10). The RICH 1 is located between the VELO and TT and is used for particles with a momentum between 2.6 and 60 GeV/c using C_4F_{10} as a reflector medium. The RICH 2 is located upstream of the ECAL and is used for higher momentum tracks between 15 and 100 GeV/c and is filled with CF_4 . The kaon identification efficiency is $\sim 95\%$ for a $\sim 5\%$ $\pi \rightarrow K$ miss identification (mis-id) probability.

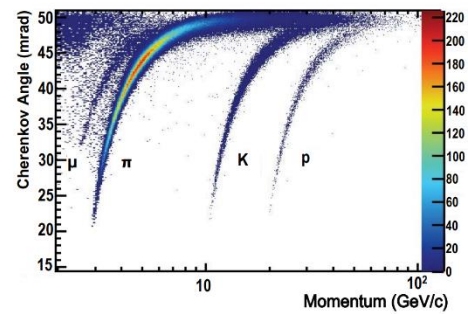


Figure 10: Correlation between Cherenkov angle and momentum [21].

The task of the ECAL and HCAL is the separation of electrons, photons and hadrons. The identification of electrons, π^0 and photons is a challenge, because the photons can interact with the detector material upstream of the calorimeters and electrons can emit Bremsstrahlung. In front of the electromagnetic calorimeter, a scintillating pad (SPD) and a pre-shower detector (PS) are installed. The SPD is used to separate electrons from photons and the PS can identify the electromagnetic character of a particle.

The muon chambers are placed at the downstream end of the detector. Only if the muons have a momentum $> 3 \text{ GeV}/c$ they can transverse the calorimeters. With a momentum $> 6 \text{ GeV}/c$ they can be tracked by all five muon chambers [22].

3.3 The trigger system

The online trigger consist of two stages: a hardware (L0) and a software (HLT≡High level trigger) stage. The different stages have strict requirements and only if they are fulfilled, the event is passed to the next trigger level (see Figure 11).

The first stage (L0) is implemented in the readout hardware of the detector and uses information from the calorimeters and the muon chambers. The L0 reduces the rate from the 40MHz bunch crossing frequency to a readout rate of 1 MHz. The second stage is a high level trigger, which is divided into two levels. In the first level (HLT1) the software uses information from the VELO and the other tracking stations to perform a partial reconstruction of trajectories of charged particles.

Here at least one track must satisfy momentum or displacement criteria. In the second level (HLT2), the full event is reconstructed and sent to the data centre for long time storage. In 2015 the final event storage rate was 12.5 kHz [24].

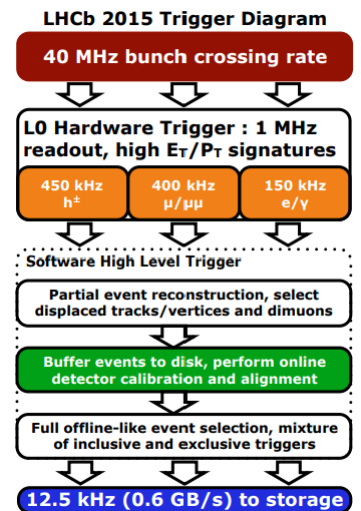


Figure 11: Trigger Diagram of the LHCb Trigger from 2015 [23].

4 Monte-Carlo simulation

This thesis uses Monte-Carlo (MC) simulation to help reducing combinatorial background. For this simulation PYTHIA, Evt-Gen and Geant4 are used to generate signal events in high energy physics. PYTHIA is an event generator for pp-collision, Evt-Gen uses information to create flavour decays and Geant4 simulates the interaction of particles with the detector. MC simulations are originally used for experiments in high energy physics, but have now gained a wide range of applications in other fields of physics, industry and engineering [25].

The simulations has been performed separately for the D and D_s signal events.

5 Measuring direct CP asymmetries

This thesis is the first step towards a direct CP measurement in the decays $D_{(s)}^+ \rightarrow K^+ \eta'$. One can calculate the CP asymmetry which is defined as

$$A_{CP} = \frac{\Gamma(D_{(s)}^+ \rightarrow K^+ \eta') - \Gamma(D_{(s)}^- \rightarrow K^- \eta')}{\Gamma(D_{(s)}^+ \rightarrow K^+ \eta') + \Gamma(D_{(s)}^- \rightarrow K^- \eta')}, \quad (7)$$

where $\Gamma(D_{(s)}^\pm \rightarrow K^\pm \eta')$ are the partial decay widths.

The production asymmetry (A_{prod}) for the $D_{(s)}^+$ and $D_{(s)}^-$ is given by

$$A_{prod} = \frac{\sigma(D_{(s)}^+) - \sigma(D_{(s)}^-)}{\sigma(D_{(s)}^+) + \sigma(D_{(s)}^-)}, \quad (8)$$

where σ is the production cross-section for the different mesons in a pp-collision and depends on the centre-of-mass energy of the collision.

In the decays studied in this analysis, the detection efficiency, ϵ , is only relevant for the kaon, since the two charged daughter pions of the η' have opposite charge and thus the effect of the detection asymmetry (A_{det}) vanishes:

$$A_{det} = \frac{\epsilon(K^+) - \epsilon(K^-)}{\epsilon(K^+) + \epsilon(K^-)}. \quad (9)$$

There are two main contributions to the detection asymmetry in the LHCb detector:

- Low momentum tracks are bent out of the detector by the magnetic field. Asymmetries in the detector geometry and acceptance can cause these charge asymmetries. When flipping polarity, this affects particles with the opposite charge.
- Different detection efficiencies for particles and antiparticles due to different material interaction properties of particles (and antiparticles) with the detector.

The observable that can be measured is the number of reconstructed D and D_s decays. A Taylor approximation can be carried out for small production and detection asymmetries:

$$A_{raw} \approx A_{CP} + A_{prod} + A_{det}. \quad (10)$$

This quantity only depends on the number of reconstructed $N(D_{(s)}^+ \rightarrow K^+\eta')$ and $N(D_{(s)}^- \rightarrow K^-\eta')$ candidates:

$$A_{raw} = \frac{N(D_{(s)}^+ \rightarrow K^+\eta') - N(D_{(s)}^- \rightarrow K^-\eta')}{N(D_{(s)}^+ \rightarrow K^+\eta') + N(D_{(s)}^- \rightarrow K^-\eta')}. \quad (11)$$

To cancel out the production- and detection asymmetry a control channel (CC) with similar production and detection asymmetries can be used. For this channel A_{CP} should be known with a higher precision than the channels that are studied in this thesis. The difference of the two raw asymmetries is

$$\begin{aligned} \Delta A_{raw} &= A_{raw}(D_{(s)}^+ \rightarrow K^+\eta') - A_{raw}(CC) \\ &= A_{CP}(D_{(s)}^+ \rightarrow K^+\eta') + A_{det}(D_{(s)}^+ \rightarrow K^+\eta') + A_{prod}(D_{(s)}^+ \rightarrow K^+\eta') \\ &\quad - A_{CP}(CC) - A_{det}(CC) - A_{prod}(CC). \end{aligned} \quad (12)$$

And the final A_{CP} can be calculated with

$$A_{CP}(D_{(s)}^+ \rightarrow K^+\eta') = \Delta A_{raw} + A_{CP}(CC). \quad (13)$$

The control channel $D_{(s)}^+ \rightarrow K_s^0 K^+$, where $K_s^0 \rightarrow \pi^+\pi^-$ will be used, since the initial and the charged final state are the same and with $A_{CP}(D^+ \rightarrow K_s^0 K^+) = (-1 \pm 7) * 10^{-4}$ and $A_{CP}(D_s^+ \rightarrow K_s^0 K^+) = (9 \pm 26) * 10^{-4}$ the CP asymmetries have small uncertainties [6].

The statistical uncertainty of $A_{CP}(D_{(s)}^+ \rightarrow K^+\eta')$ is calculated using the assumption that the final $A_{CP} = 0$ and therefore $N(D_{(s)}^+) = N(D_{(s)}^-)$. This assumption is assumed to be valid, since from theoretical predictions the A_{CP} in charm decays is very small:

$$\begin{aligned} \sigma_{stat}(A_{CP})_{A_{CP}=0} &= \sqrt{\left(\frac{\partial A_{CP}}{\partial N^+}\right)^2 \sigma^2(N^+) + \left(\frac{\partial A_{CP}}{\partial N^-}\right)^2 \sigma^2(N^-)} = & (14) \\ &= \sqrt{\frac{4(N^-)^2}{N_{sig}^4} \sigma^2(N^+) + \frac{4(N^+)^2}{N_{sig}^4} \sigma^2(N^-)} = \sqrt{\frac{\sigma^2(N_{sig})}{N_{sig}^2}} = \frac{\sigma(N_{sig})}{N_{sig}}. \end{aligned}$$

Here, N^+ is the number of reconstructed D^+ or D_s^+ and N^- is the number of reconstructed D^- or D_s^- decays. Since this analysis is not probing the charge of the $D_{(s)}$ the number of obtained signals N_{sig} is given by $N_{sig} = N^+ + N^-$. And with the assumption of $A_{CP} = 0$ this reduces to $N^+ = N^- = \frac{N_{sig}}{2}$.

In Equation (14) N_{sig} denotes the signal yields of the fit and $\sigma(N_{sig})$ denotes the uncertainty of the signal yields in the fit, which is calculated separately for D and D_s mesons.

6 Data set and trigger selection

The data set used in this analysis was taken during Run2 of the LHCb experiment, from 2015 to 2018, with a centre-of-mass energy of $\sqrt{s} = 13$ TeV, corresponding to a time integrated luminosity of $5.7fb^{-1}$ [26] (see Table 4). The magnet polarity was regularly flipped during Run2 to correct for the detection asymmetry (see section 5).

Table 4: Integrated luminosities of LHCb: Separated for different years of Run2.

Year	2015	2016	2017	2018	total
Integrated luminosity [fb^{-1}]	0.30	1.6	1.7	2.1	$\Sigma = 5.7$

It was decided to not use data from Run1 because only inclusive trigger lines for D mesons were implemented. These inclusive trigger lines only reconstruct a particle and not a complete decay and have therefore a lower efficiency.

6.1 The trigger

There are two fundamental non exclusive trigger decisions in the LHCb trigger [27]:

- TIS (Trigger independent of signal) events:
These events are triggered independently of the presence of the signal. A candidate is considered to be TIS with respect to a trigger selection if removing it from the event would still cause the trigger selection to accept the event, i.e. if the other particles in the event are sufficient to satisfy the trigger selection.
- TOS (Trigger on signal) events:
These are events triggered on the signal decay chain independently of the presence of other tracks. This condition is fulfilled if the information used to reconstruct the signal tracks is sufficient to satisfy the selection criteria of the respective trigger line.

6.1.1 The trigger selection

To avoid biases for the final CP asymmetry, it is important that one differentiates between a positive and a negative charged particle (for the $D_{(s)}^+$ and $D_{(s)}^-$ meson) only at the end of the analysis. To calculate A_{raw} the number of reconstructed decays for $D_{(s)}$ is measured. The charge of the $D_{(s)}$ meson is determined by the charge of the kaon. This is the reason why the $D_{(s)}$ meson is triggered TIS and the η' meson can be triggered TOS.

6.1.1.1 L0 trigger

In general the D meson can be triggered at the L0 stage by any of the requirements listed in Table 5. In this analysis it was decided to trigger the D meson TIS. The η' meson is triggered by the hadronic requirement from Table 5 and is triggered TOS.

Table 5: Thresholds for the L0 trigger.

	hadronic	muonic		electromagnetic		
		μ	$di - \mu$	e	γ	π^0
<i>threshold</i>	3.5	1.3	$\Sigma > 1.5$	2.6	2.3	4 – 4.5
$\frac{p_T}{E_T} [1/c]$						

6.1.1.2 HLT1 trigger

The HLT1 trigger line uses the partial reconstruction of an event by adding information from the VELO or the main tracker and applying cuts on the p_T and IP with respect to the primary vertex. In this analysis, the daughter pions of the η' are triggered by the dedicated HLT1 stage by finding two pions with the same origin vertex or just by applying the trigger selection to a pion in general. A trigger line is a sequence of algorithms returning a decision to accept or reject an event according to a particular event topology.

6.1.1.3 HLT2 trigger

For the HLT2 the complete event is reconstructed by reconstructing composite particles first and then reconstructing two different types of selections. The inclusive selection is used mainly for calibration tasks and the exclusive selection is used for a full reconstruction of an event of interest with the highest possible efficiency. In this analysis an exclusive trigger selection is applied. The selection criteria (pre-cuts) for this HLT2 line are listed in Table 6. [28]

Both the MC and the data sample are based on this HLT2 trigger line. The trigger lines for the different trigger levels from section 6.1.1 are summarised in Appendix A.

Table 6: Pre-cuts from the trigger-line.

Particle	Variable	Selection
$D_{(s)}$	m	$\in [1600,2200] \text{ MeV}/c^2$
	p_T	$> 2000 \text{ MeV}/c$
	χ^2_{vtx}/ndf	< 5
	τ	$> 0.25 \text{ ps}$
	$\chi^2/ndf (DTF_{PV})$	< 4.5
K	p	$> 1000 \text{ MeV}/c$
	p_T	$> 600 \text{ MeV}/c$
	χ^2_{IP}	> 25
	χ^2_{trk}	< 5
	P_{Ghost}	< 0.5
η'	m	$\in [860,1060] \text{ MeV}/c^2$
γ	p_T	$> 1000 \text{ MeV}/c$
$\pi^+\pi^-$	m	$\in [200,1200] \text{ MeV}/c^2$
π^\pm	η	$\in [2,5]$
	p	$\in [1000,100000] \text{ MeV}/c$
	$DLL_{K\pi}$	< 0
	p_T	$> 500 \text{ MeV}/c$
	χ^2_{IP}	> 25
	χ^2_{trk}	< 5
	P_{Ghost}	< 0.5

7 General overview of the analysis

The invariant mass distribution of the D meson is evaluated using a DTF and is plotted in Figure 12 with the pre-cuts applied.

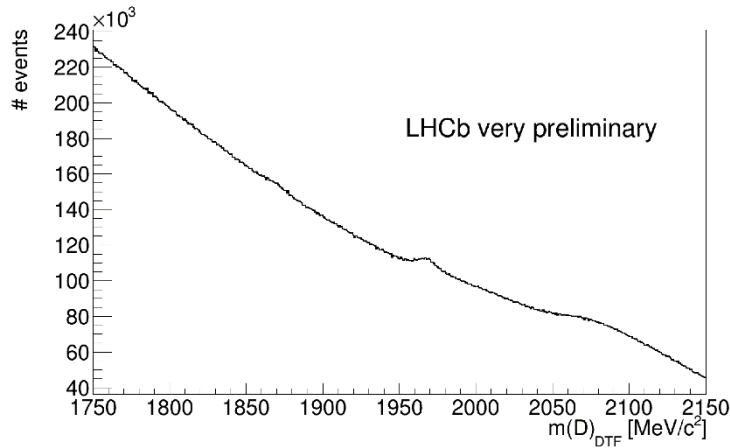


Figure 12: D mass distribution with pre-cuts applied.

The distribution is clearly dominated by background, since there are only barely visible peaking structures around the mass of the $m(D^+) = 1869.66 \text{ MeV}/c^2$ and $m(D_s^+) = 1968.35 \text{ MeV}/c^2$.

The goal of this analysis is to identify and reduce the background and optimize the selections in order to achieve the most precise measurement of A_{CP} .

The selection consists of two stages: an offline selection and a BDT selection. The offline selection is applied before training the BDT and the BDT selection consists of a cut on the BDT output and the η' mass. The final selection consists of the final chosen BDT output and $m(\eta')$ cut.

8 Secondary decays

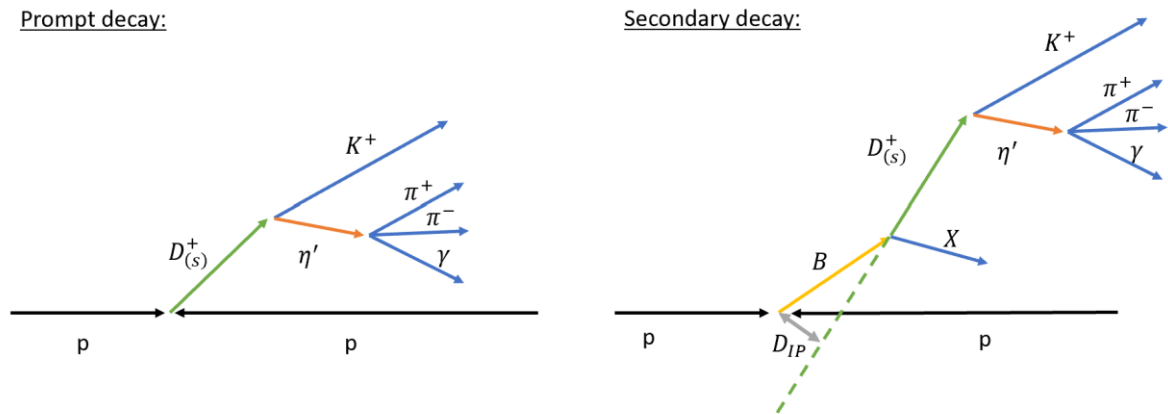


Figure 13: Difference between the impact parameter (grey) of the D meson (green) of a prompt (left) and a secondary decay (right). The B meson (yellow) at the right can decay into the D meson and some other particles called X .

To be sure that the decay of interest has its origin at the PV, a cut on the χ_{IP}^2 of the D meson can be applied. The χ_{IP}^2 is a good variable to separate D mesons directly produced in the pp-collision (prompt decays) from D meson decays from B decays (secondary decays) (see Figure 13), since a secondary decay has a larger impact parameter than a prompt decay.

With a cut on χ_{IP}^2 possible secondary decays, where a B meson or a baryon is produced in the PV and decays afterwards into a D meson, can be cancelled out. The final CP asymmetry for these two types of production is the same, but the production asymmetry for D and B mesons in a pp-collision is different. Thus, secondary decays are treated as background in most LHCb measurements which analyse CPV in the charm sector. By reducing the contamination of secondary decays, this bias can be reduced.

8.1 Selection for a cut on the impact parameter

The fraction of secondary decays can be obtained by comparing the χ_{IP}^2 of prompt and secondary produced D mesons in the simulated data only with the pre-cuts applied (see Figure 15). When comparing the ratio between the number of secondary decays and the number of total decays, it must be smaller than 10% in order to have control of the

systematic uncertainties. To select the χ_{IP}^2 that satisfies this criterion a scan for different cuts on $\log(\chi_{IP}^2)$ is performed (see Table 7 and Figure 14).

Table 7: Scan of the contamination of secondary decays. Number of total decays = number of secondary decays + number of prompt decays.

$\log(\chi_{IP}^2)$	$\frac{\# \text{ secondary decays}}{\# \text{ total decays}} [\%]$
no cut	14.09
< 8	14.06
< 6	13.84
< 4	13.80
< 3	13.43
< 2.5	10.98
< 2.3	9.96
< 2	8.57
< 1.5	6.71
< 0	4.37
< -3	3.77

The cut $\log(\chi_{IP}^2(D)) < 2$ with a contamination of 8.6% of secondary decays will be used. The contamination is smaller than 10% and the cut does not reduce the number of total events too much (see Figure 16).

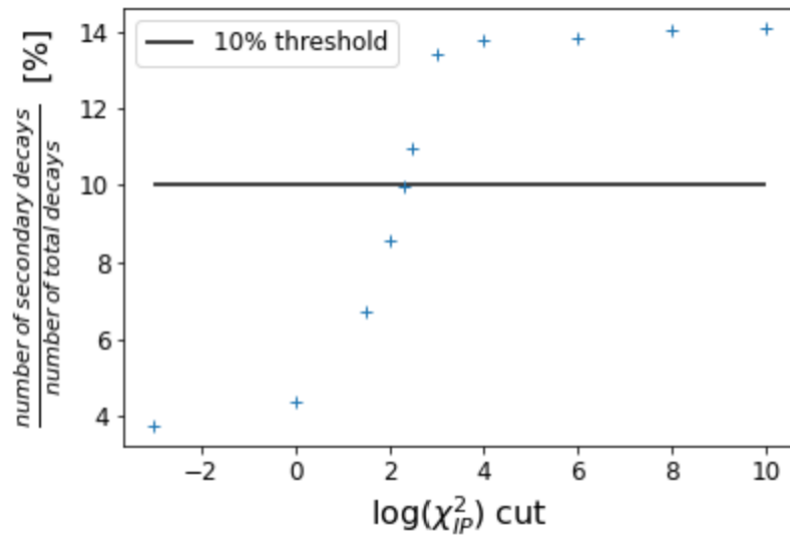


Figure 14: Fraction of secondary decays against cut on $\log(\chi_{IP}^2)$ of the D meson. Values from Table 7 only with pre-cuts applied.

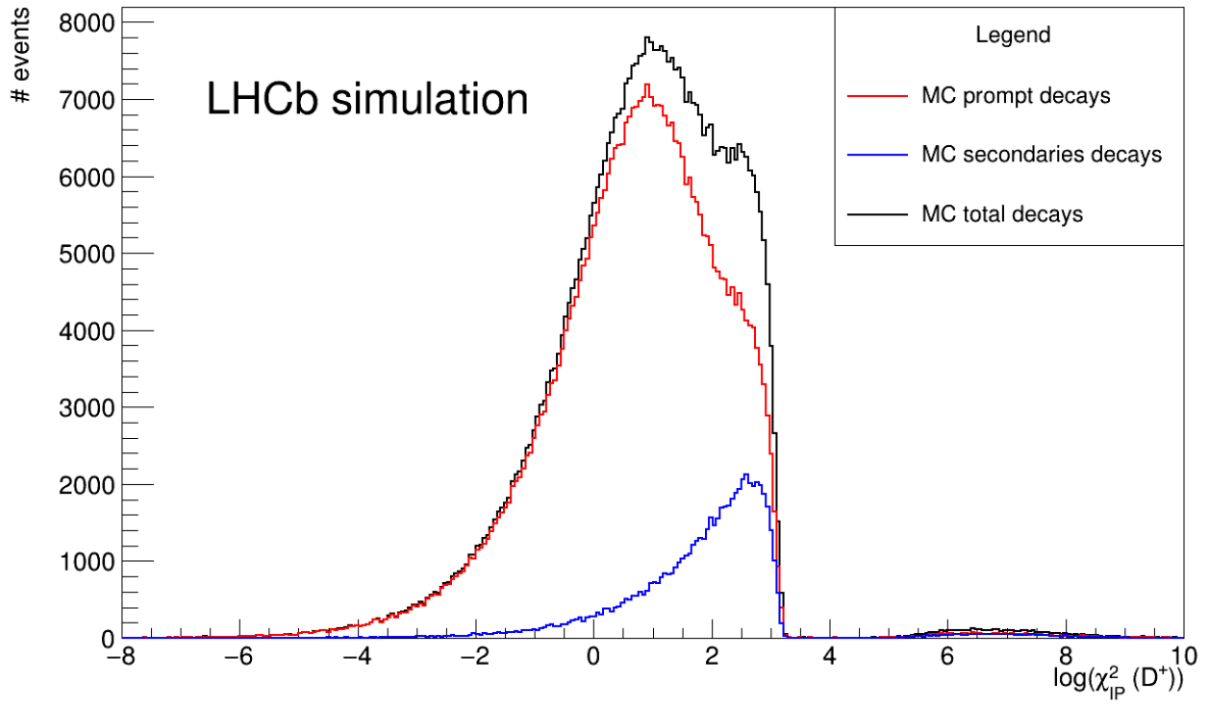


Figure 15: Comparison of the $\log(\chi^2_{IP})$ of prompt (red), secondary (blue) D decays and the sum of both (black) from the MC sample only with pre-cuts applied.

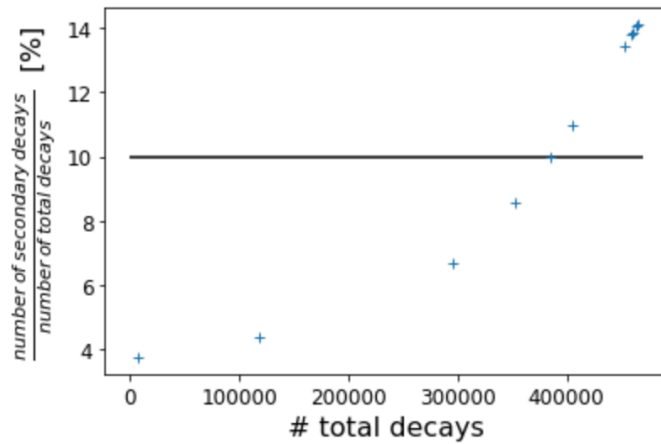


Figure 16: Fraction of secondary decays in percent against total number of decays for the MC simulated data only with pre-cuts applied.

8.2 Estimate on the impact of secondary decays to the systematic uncertainty

To understand the influence of secondary decays to the systematic uncertainty in more detail, one can have a look at the shift in the raw asymmetry. The shift in the raw asymmetry due to the difference between the production asymmetry of the D and B mesons is

$$A_{eff}^{prod} = (1 - \Sigma f_i) * A_{D(s)}^{prod} + \Sigma(f_i * A_i^{prod}).$$

Here, f_i is the fraction of the number of decays with a specific B meson mother particle involved and the total number of secondary decays. Since the production asymmetry for B_s^0, B^0, B^+ and Λ_b are only measured at $\sqrt{s} = 7$ TeV, the values are listed in Table 8 [29].

Table 8: A^{prod} of b hadrons.

<i>Mother particle</i>	A^{prod} [%]
B_s^0	$(0.44 \pm 0.88 \pm 0.11)$
B^0	$(-0.65 \pm 2.8 \pm 0.59)$
B^+	$(-0.23 \pm 0.24 \pm 0.37)$
Λ_b	$(-0.11 \pm 2.53 \pm 1.08)$

The production asymmetry for the D and D_s meson for $\sqrt{s} = 7$ TeV are given by

$$A_D^{prod} = (-0.96 \pm 0.26 \pm 0.18)\% [30],$$

$$A_{D_s}^{prod} = (-0.52 \pm 0.13 \pm 0.10)\% [31].$$

The cut $\log(\chi_{IP}^2(D)) < 2$ has a contamination of 8.6%, which results into $f \approx 8.6\%$ and a $A_i^{prod} \approx 1\%$, since the values in Table 8 have a large uncertainty. This leads to a maximal bias of $1\% * 8.6\% = 0.086\%$.

This is just a first rough estimate of the systematic uncertainty and the investigation is mainly done for selecting a cut on χ_{IP}^2 for the offline selection (see section 9.2). For a full study of the systematic uncertainty, the contamination after the final selection has to be taken into account.

9 MVA classifier

To reduce combinatorial background the correlation between different input variables must be considered. Combinatorial background consists of random combination of tracks that form a signal.

The Multivariate Data Analysis Toolkit [32] is a program that uses a multivariate analysis method that can evaluate different input parameters at the same time. A univariate analysis uses only one input instead.

9.1 BDT classifier

The Boosted Decision Tree (BDT) is an algorithm that uses a binary (yes/no) criterion in a decision tree to classify an event as signal or background.

From the root node, the separation starts into two new nodes. The yes/no decision on one variable at each split is repeated iteratively until a stop criterion is reached. After each node the variable with the best separation power between signal and background is chosen as variable to cut on.

In this way the n -dimensional phase space (n =number of input variables) is separated into a number of regions that are classified as signal or background. This classification is depending on the number of training events that reached these “leaves” in the training stage. A typical decision tree model is shown in Figure 17.

For boosting the decision tree there are a number of Boost types. In the AdaBoost (adaptive boosting) the boost is performed by giving higher weights to misclassified events. Misclassified events are events, which end up in the “wrong” leaf (e.g. a signal event that ends up in a background leaf). In the next step, a new decision tree is created and it uses the new weighted training sample. This decision tree will try to separate the previously misclassified events harder. This is performed iteratively and in the end all decision trees (called a forest in total) are averaged. This should ensure that fluctuations in the input data are not trained as features

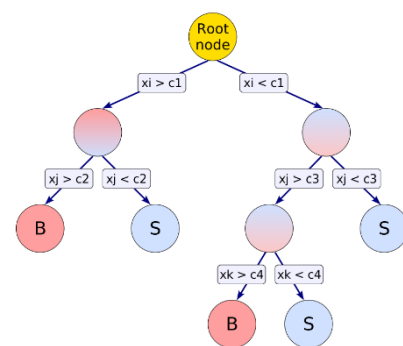


Figure 17: Decision tree [24].

of the signal/background. Another boost type is the gradient boosting where the residuals between a decision tree and the best possible model are used to describe the imperfections of the current decision tree. In an iterative fashion this can be repeated, until a stop criterion is fulfilled.

The definitions of some parameters of the BDT are listed in Table 9.

Table 9: Definition of the parameters in the BDT.

BDT parameter	Definition
BoostType	Which type of boosting is used
NTrees	Number of trees in the forest
MaxDepth	Maximal depth of one decision tree
nCuts	Number of possible cuts per variable
NodePurityLimit	If a node has purity > NodePurityLimit it is classified as signal
MinNodeSize	Minimal percentage of training data events required in one leaf

The process of a BDT is performed in two stages: the training/testing and the application stage. In the first stage the BDT is trained using data samples which include pure background and signal events. It is tested afterwards with similar signal and background samples to test the robustness of the algorithm. In the application stage, an unknown data sample (in terms of signal and background) is given to the trained BDT. The BDT selects data points in this sample as signal and background by comparing in which leaf the data point ends.

A critical point in MVA is the problem of overtraining. When the algorithm has only a few degrees of freedom and the training sample is relatively small, the BDT response for the training and test sample can drastically differ due to the statistical process of the BDT. BDTs are more prone to overtraining than other classifiers because they have a large number of nodes. To test if a classifier is overtrained, the Kolmogorov-Smirnov test (KS test) can be used [33]. This test is used to compare two probability distributions by comparing the maximal difference

in the cumulative sum of two distributions. To perform this test, the data after the offline selection is separated into a training and a testing part. The training part contains the same amount of “signal” and “background” data and is used to train the BDT. After the training, the BDT is applied to the other part of the data sample (testing part). The p-value of the KS test is a number between 0 and 1, for signal and background each. A small p-value is an indicator to reject the null-hypothesis (in this case the classifier responds from the training sample). It is only of interest, that the p-value is sufficiently large, but it contains no information about the probability, that the two distributions are the same.

9.2 Offline selection

To reduce the background, some offline selection cuts are applied to the data and MC samples before splitting the data and MC samples into training and testing samples. These cuts are used to reduce background before the BDT is used.

As discussed in section 3.2, only particles with a pseudorapidity between 2 and 5 are detected by the LHCb detector. These fiducial cuts are implemented in the trigger but to be sure, a cut is used again on the pseudorapidity of the D and K . In the MC simulation a γ_{CL} between 0 and 1 is allowed, but the pre-cut of the data is > 0.8 . Because the γ_{CL} is a potential candidate for an input variable of the BDT, the distributions from the data and MC samples need the same domain. Thus a cut on $\gamma_{CL} > 0.8$ is applied.

To reduce background, where a pion is misidentified as a kaon, the cut $DLL_{K\pi} > 8$ for the kaon is applied (detailed explanation how this cut is determined in section 10). The cut on the invariant mass of the two daughter pions of the η' meson $m(\pi^+\pi^-) > 600 \text{ MeV}/c^2$ reduces background, because $\eta' \rightarrow \rho^0(\rightarrow \pi^+\pi^-)\gamma$ dominates the decay. To remove background where a random photon is accidentally included in a reconstructed event, a cut on the invariant mass of the daughter pions of the η' and the kaon $m(\pi^+\pi^-K^+) < 1825 \text{ MeV}/c^2$ is sufficient [34]. Plots to motivate these cuts are plotted in Appendix B. Cuts on the transverse momentum of the D and K will remove combinatorial background, because these particles usually have a lower transverse momentum distribution.

In a MC simulation, an entire pp-collision is simulated and then a trigger line selects the decay of interest. Nevertheless, it can happen that a random track is selected as signal. With truth matching this background is removed and it is only possible with simulated data, since each particle is exactly known. To the MC simulated data, a truth matching is applied.

All offline cuts are listed in Table 10.

In the data from 2015 to 2017, there are only events with one PV due to an error in the trigger selection. In the 2018 data these trigger lines changed and events with more than one PV could pass the trigger. In the MC samples from 2016-2017, there are only events with one PV too and for 2018 more than one PV is possible.

Multiple PVs per event can be explained by multiple pp interactions per bunch crossing. This analysis does not use MC simulations from 2015, because these MC samples are not available. However they should be similar to the MC sample of 2016.

The invariant mass distribution of the D meson with the applied offline selection cuts can be seen in Figure 18. The distribution has a parabolic background shape. After the offline selection the peak around the D_s mass is clearly visible and a small peak can be seen around the D mass. The distribution with the pre-cuts (see Figure 12) has a structure at $2070 \text{ MeV}/c^2$, which is not visible anymore after the offline selection. The background, especially in the high mass region closest to the upper end, is heavily reduced.

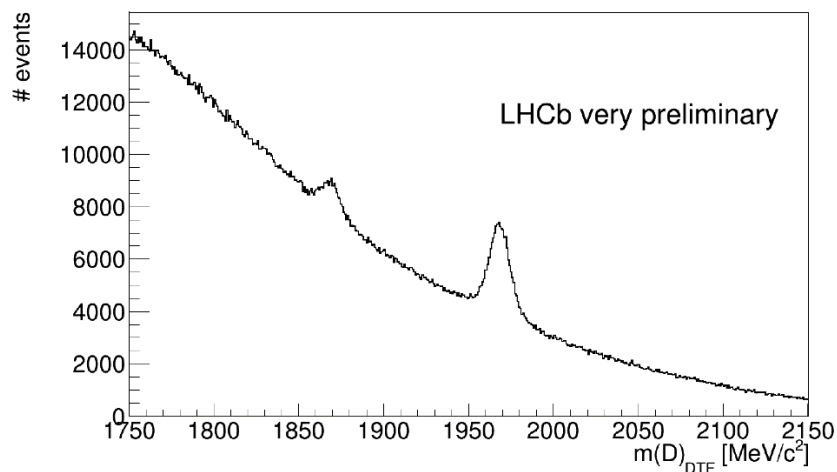


Figure 18: D mass distribution with offline selection cuts applied.

Table 10: Summary of offline selection cuts. Definition of the variables in: List of abbreviations.

Particle	Variable	Cut before BDT training
<i>MC simulation</i>	truth matching	Only for MC sample (See [35] for the numbers)
<i>Trigger lines</i>	Explained in section 6.1.1	Summarised in Appendix A
γ	γ_{CL}	> 0.8
	$\gamma_{isPhoton}$	> 0.6
K	$DLL_{K\pi}$	> 8
	η	$\in [2,5]$
	p_T	$\in [1000,20000]$ MeV/c
D	$\log(\chi_{IP}^2)$	< 2
	η	$\in [2,5]$
	p_T	$\in [2700,20000]$ MeV/c
	$m(\pi^+\pi^-K^+)$	< 1825 MeV/c ²
η'	$m(\pi^+\pi^-)$	> 600 MeV/c ²

Table 11: Total number of events before and after the offline selection.

	background	signal
Before the offline selection	$62.38446 * 10^6$	$4.65121 * 10^6$
After the offline selection	$2.905284 * 10^6$	$0.061349 * 10^6$

The total number in the data and the simulation data sets before and after the offline selection are listed in Table 11.

9.3 Input variables of the BDT

This analysis uses kinematic variables as input parameters to separate background from signal. The χ_{IP}^2 of the kaon and the pion and the $\chi_{ENDVERTEX}^2$ of the D meson are used to properly reconstruct a primary decay. The flight distance of the D meson shows a visible difference between signal and background data (see Figure 19).

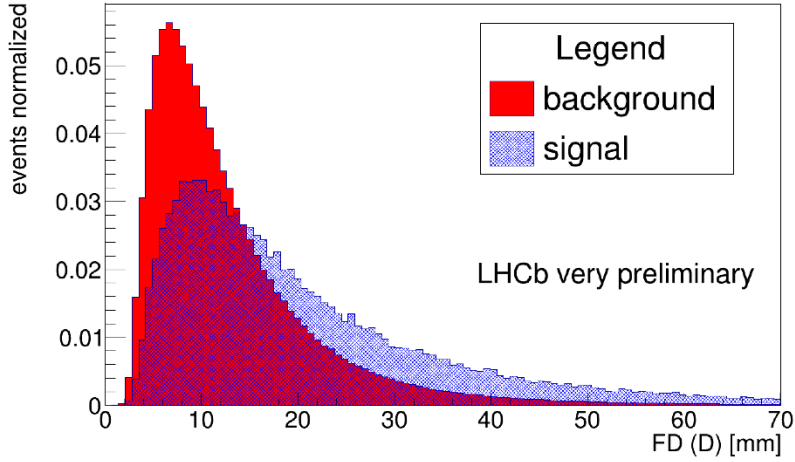


Figure 19: Flight distance of the D meson. Background (red) and signal (blue) are plotted normalized to unit area.

The χ^2_{IP} of the D meson has a different distribution for background and signal, but this variable was not used because it can be used to separate primary from secondary decays. This separation is important for further studies of systematic uncertainties, and is therefore already included in the offline selection.

For the two daughter pions of the η' (π^+ and π^-), an extra strategy is needed to reduce the number of possible variables in the BDT because a larger number of input variables can cause overtraining of the BDT. To reduce the number of variables the maximum of a parameter of the two pions can be used. For a variable x , the input variable for the pions is defined:

$$x(\pi^\pm) := \max(x(\pi^+), x(\pi^-)).$$

The DLL values remove background from misidentification. For example, the $DLL_{K\pi}$ distribution of the pions for signal and background (see Figure 20) is separated well in comparison to the other variables.

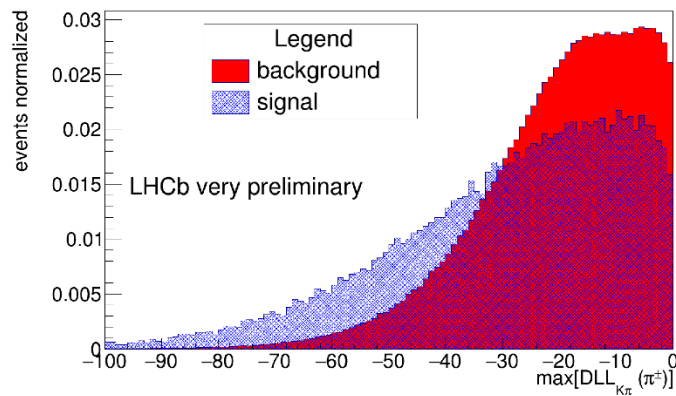


Figure 20: Maximum of $DLL_{K\pi}$ of the two pions. Background (red) and signal (blue) are plotted normalized to unit area.

A DLL value of the kaon instead, when used in the classifier, can induce a bias in our analysis, since it is used to determine the charge of the D meson. All input variables that are considered and which of them are used in the final BDT are listed in Table 12.

All normalized distributions of signal and background for the input parameters after the offline selection are plotted in Appendix D.

Table 12: Input variables for the BDT. Definition of the variables in: List of abbreviations.

Particle	Variable	Present in the final BDT
D	p_T	
	p	
	$\chi_{ENDVERTEX}^2$	
	Θ_{DIRA}	x
	$\chi_{PVFitBeam}^2$	
	FD	x
γ	γ_{CL}	
	p_T	x
η'	χ_{FD}^2	x
K^\pm	$\chi_{trk}^2/ndof$	x
π^\pm	$DLL_{p\pi}$	x
	$DLL_{K\pi}$	x
	$DLL_{e\pi}$	
	$DLL_{\mu\pi}$	
	p_T	
	χ_{IP}^2	x
	$\chi_{trk}^2/ndof$	x
	P_{Ghost}	x

9.3 Training samples

The BDT needs to be trained to learn how to differentiate between signal and background. For this reason, the training signal sample should include a mainly pure signal and the training background sample should include mainly pure background. For the signal sample the MC simulated data is chosen, because true decays are used.

For the background sample the data sample with an additional cut on the η' mass is used. The cut for $m(\eta') \notin [905, 1009] \text{ MeV}/c^2$ is chosen by fitting a gaussian to the η' mass data for the

total dataset (with only L0 trigger, HLT1 trigger, HLT2 trigger and D/K pseudorapidity cuts applied) and cutting out an interval around the mean with a width of $\pm 4\sigma$ (see Appendix C).

For the training of the BDT the data and simulations from all years are added up. So in the end the BDT is trained only with one background and one signal sample.

The offline selection cuts listed in Table 10 are applied.

9.4 BDT parameter scan

To find the optimal BDT parameters the BDT was trained several times and the options BoostType, NTrees, MaxDepth, nCuts, NodePurityLimit and MinNodeSize are changed. To evaluate the impact of the different changes the area under the ROC-curve (receiver operating characteristic curve), the presence of overtraining and the shape of the BDT response are compared. The ROC-curve compares the background rejection ($1 - \text{background efficiency}$) against the signal efficiency [36]. The goal is to reduce the background by minimal loss of the signal. So, a high signal efficiency with a high background rejection at the same time is needed.

First, the two Boost types AdaBoost (adaptive boosting) and Grad (gradient boosting) are compared. The number of trees in the forest (NTrees) is varied between (300, 400, 500, 600), for the maximal depth of one decision tree (MaxDepth) the scan is performed between (2, 3, 4) and the minimal percentage of training data events required in one leaf (MinNodeSize) is chosen between (4%, 5%, 6%). The number of possible cuts per variable (nCuts) and the NodePurityLimit (if a node has a purity $>$ NodePurityLimit it is classified as signal) are changed but the default values of 20 and 0.5 give the best result for the ROC-value (see Appendix E). For the normalisation of the signal and the data, the number of events is used and the data samples are split randomly to reduce possible training of features that are not typical for the signal or background.

At the end, the values (Grad, 400, 2, 5%) for the configuration discussed above are used with an integrated ROC-curve value of 0.850 (see Appendix E).

The BDT output, after applying the BDT to the data with the offline selection applied, can be seen in Figure 22 and the normalized BDT response for the training and testing data with the p-value from the KS test is plotted in Figure 21.

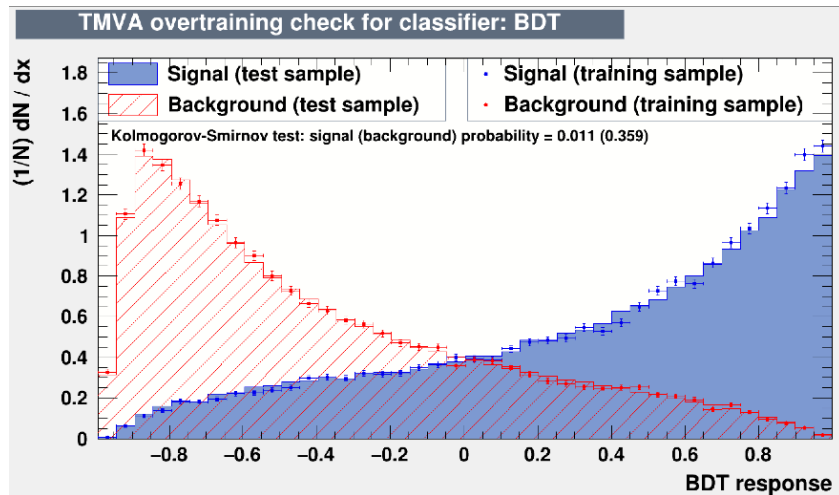


Figure 21: Signal (blue) and background (red) distribution of the BDT after training (filled) and testing (points).

The BDT response is maximal close to the edge of the BDT responses range. The background component is located more at negative values and the signal at positive values. Most of the background component is concentrated between -1 and -0.4 (see Figure 21). This plot is normalized. The background sample is much larger than the signal sample, so a small tail of the background in the signal region has a large impact.

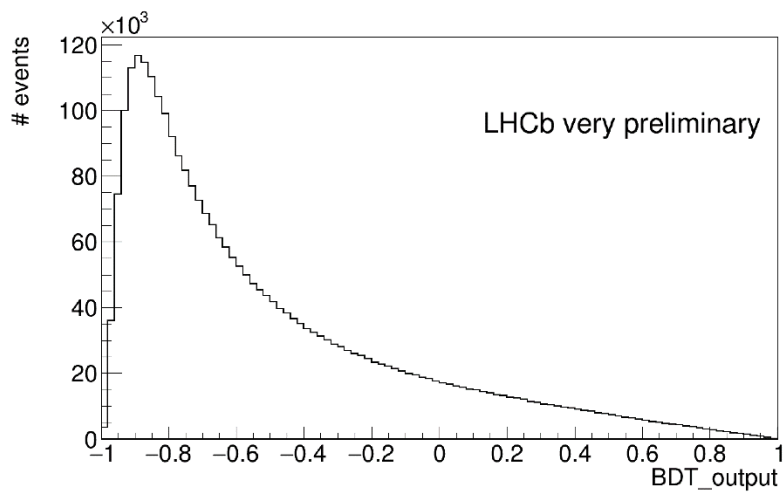


Figure 22: BDT output after applying the BDT to the data set with the applied offline selection cuts.

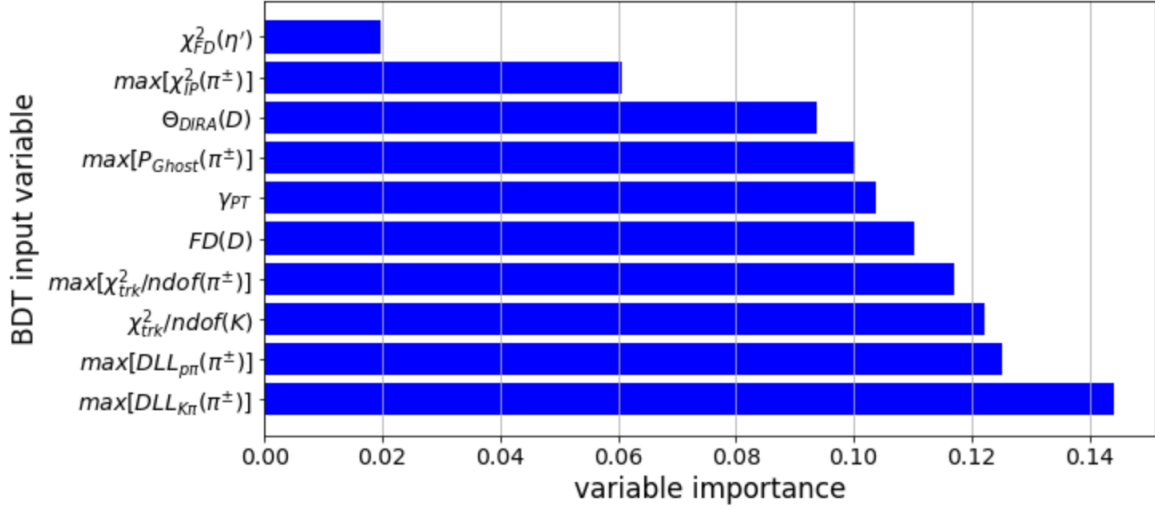


Figure 23: BDT input variables sorted in order of the importance in the BDT classifier.

The BDT is first trained with seventeen variables and to avoid overtraining, only the ten variables with the highest importance are selected and the scan for the parameters is repeated (see Table 12). The importance of a variable in the BDT is measured by calculating how often a cut on a variable is chosen. The importance of the flight distance of the η' is minor compared to the other variables (see Figure 23). When taking the variable out of the BDT, the remaining nine variables are split into two groups (one with higher and one with lower importance than before). The p-value of the Kolmogorov-Smirnov test gets smaller.

9.5 Cut on the output of the BDT

The best cut on the BDT output is chosen by maximizing $\frac{S}{\sqrt{S+B}}$ (S = number of signal events and B = number of background events). It is equal to $1/\sigma_{stat}(A_{CP})$ (taken from Equation (14) in section 5) and is used, since this quantity can be directly extracted from the fit. After the offline selection and the BDT, a scan with different $m(\eta')$ intervals ($1, 1.5, 2\sigma$) and different BDT cuts (from -1 to 0.9 in steps of 0.1) is performed and the goal is to find a BDT cut, where $1/\sigma_{stat}$ of the D and D_s signals are large (corresponding to a small statistical uncertainty of A_{CP}) at the same time (see Appendix F). This is realised by fitting two gaussians with a second order Chebyshev polynomial background component in the range of $m(D)_{DTF} \in [1840, 2010] \text{ MeV}/c^2$. The $1/\sigma_{stat}$ - distributions of the scan for the D and D_s signal are plotted against the BDT cut (Figure 24 and Figure 25).

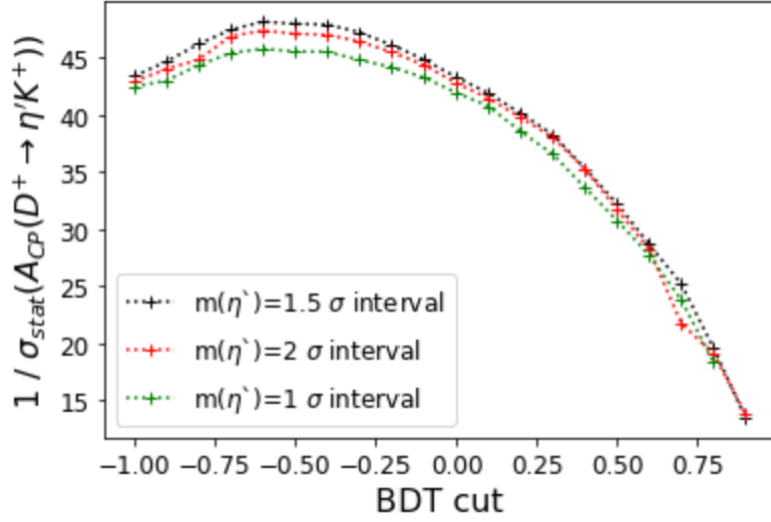


Figure 24: $1/(\sigma_{stat}(A_{CP}(D^+ \rightarrow \eta' K^+)))$ against BDT cuts for different $m(\eta')$ intervals.

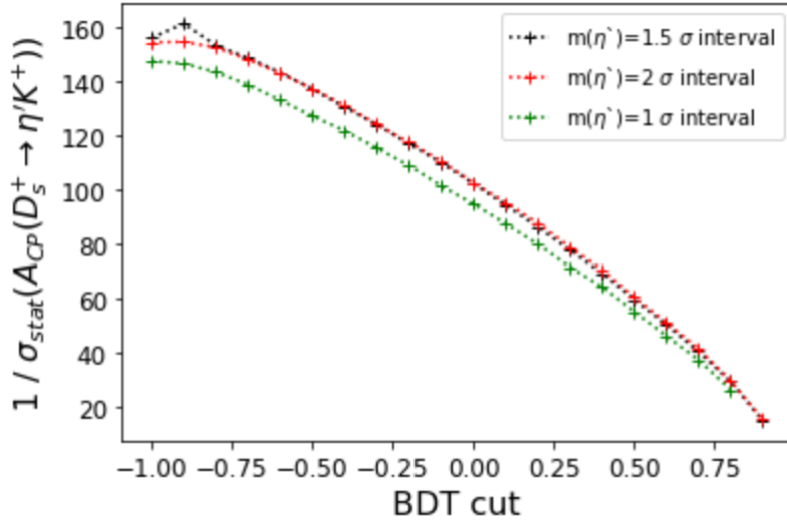


Figure 25: $1/(\sigma_{stat}(A_{CP}(D_s^+ \rightarrow \eta' K^+)))$ against BDT cuts for different $m(\eta')$ intervals.

When cutting on small values of the BDT cut, the invariant mass distribution is dominated by background and this has a negative impact on the resolution of the signal peaks that are fitted. For larger BDT cuts the distribution contains only signal, but the total number of events is so small that the statistical uncertainty gets too large. A similar behaviour is expected for the cut on the η' mass. For a tight cut around the fitted mass peak, the statistics are lower and for a looser cut the signal is contaminated more by background decays.

For a more advanced study the $D_{(s)}$ mass distribution and the η' mass distribution can be fitted simultaneously for a better separation between signal and background.

One can see such a behaviour for the resolution of the number of reconstructed D mesons. There, the best BDT cut is around -0.5 and $m(\eta') \in 1.5\sigma$ interval which is in the middle of a small plateau, where $1/\sigma_{stat}$ is at a maximum (see Figure 24). For the fit of the D_s mass, only a small improvement at very low BDT cut is visible and for larger $m(\eta')$ intervals the $1/\sigma_{stat}$ - distribution stays the same. A possible outlier is a maximum at a BDT cut of -0.9 and a 1.5σ interval of the η' mass (see Figure 25).

This behaviour for the D_s is not expected, and it is studied by varying parameters in the BDT and checking for possible errors in the fit (convergence and a positive definite covariance matrix). To understand this problem better, a plot of several mass distribution plots for different BDT cuts are plotted normalized in Figure 26.

In Figure 26 it can be seen that the signal purity for the D and the D_s signal increases with larger BDT cuts, because the height of the signal peaks increases and the background stays at the same level in the normalized plots. In Figure 27 the same mass distributions from Figure 26 are plotted but not normalized. Here the outlier from Figure 25 is plotted in black. It can be seen, that in comparison between the yellow and the black distribution the background under the D_s signal is reduced and the signal peak height is similar. In general, the background on the lower mass

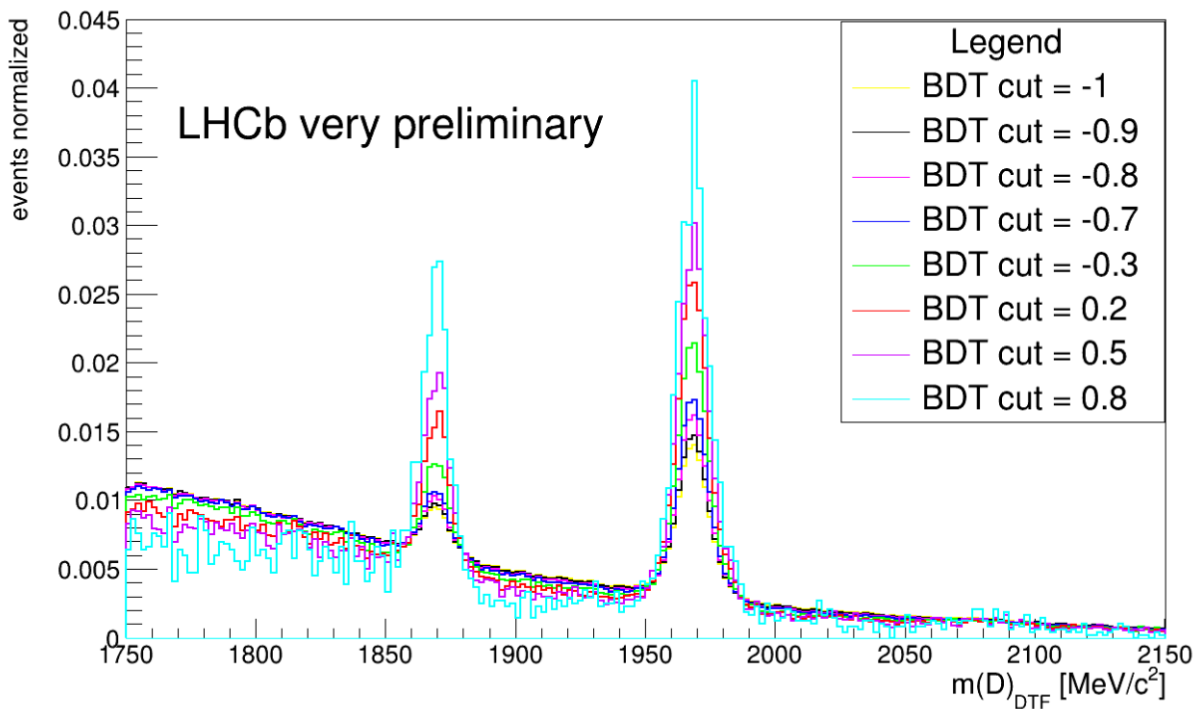


Figure 26: Plot of $m(D)_{DTF}$ normalized for different BDT cuts and a cut on $m(\eta')$ in a 1.5σ interval.

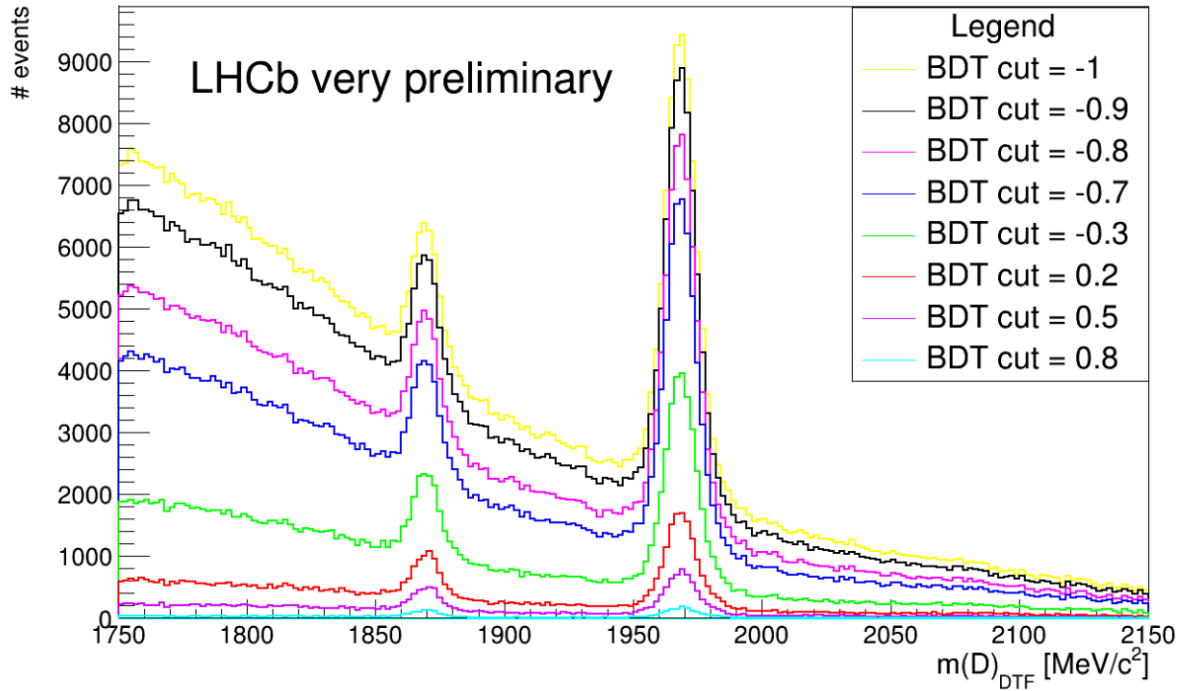


Figure 27: Plot of $m(D)_{DTF}$ for different BDT cuts and a cut on $m(\eta')$ in a 1.5σ interval.

range around the D signal is reduced for a BDT cut from -1 to -0.3, but the number of D/D_s signals stays nearly constant. For the D_s signal the signal peak height decreases more rapidly.

It can be concluded from Figure 26 and Figure 27 that the BDT is more sensitive to the separation of the D signal from the background than the separation of the D_s signal from the background. An explanation for this could be a difference in the MC simulations for the D and D_s signals.

Another possibility to investigate the difference between the different behaviour of the $1/\sigma_{stat}$ - distributions of the D and D_s signals is a two dimensional plot, where the mass of the η' is plotted on the y axis and the mass of the $D_{(s)}$ meson is plotted on the x axis. Because in Figure 24 and Figure 25 it was decided to apply a cut on the η' mass, these kind of plots will help to understand what is the motivation behind these cuts and if they are justified.

For a good separation between signal and background, two ellipse shaped areas with a high amount of events with means at the corresponding PDG values of the D and D_s mass on the x axis and at the PDG values for the η' mass on the y axis are needed.

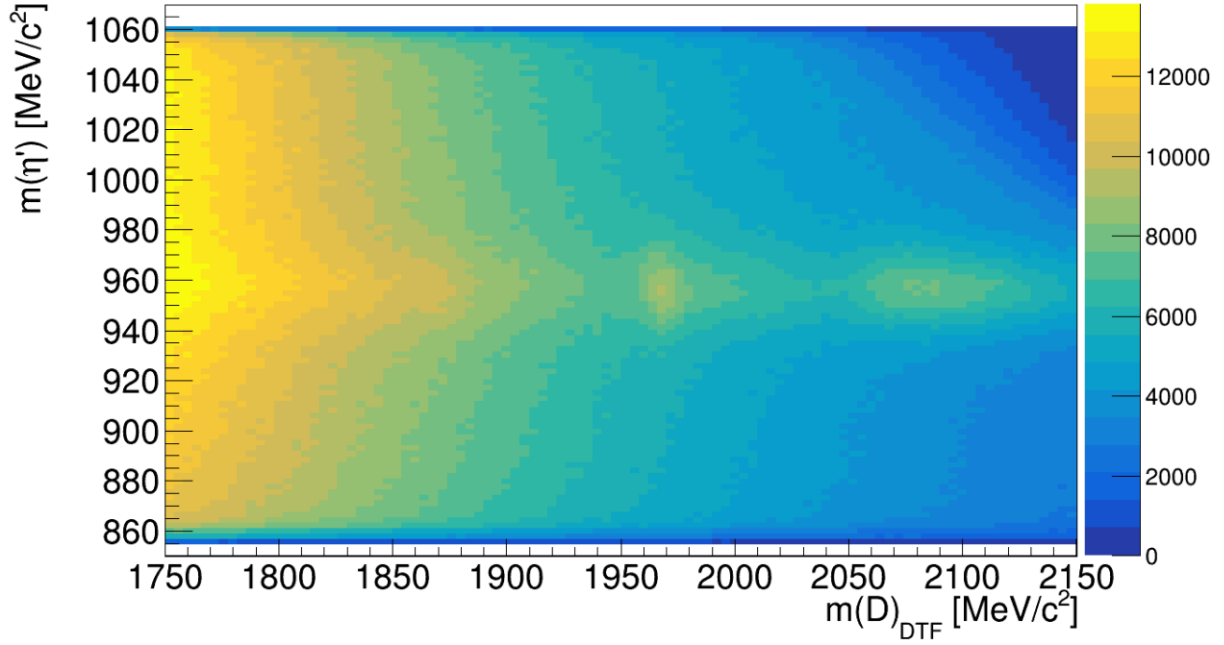


Figure 28: Scatter plot of $m(\eta')$ on the y axis and $m(D)_{DTF}$ on the x axis of the data sample only with pre-cuts applied.

In Figure 28, only the pre-cuts are applied. It can be seen that the sample is dominated by background and only a small peak for the D_s signal is visible. Most of the background is located at a mass range between 1750 MeV/c² and 1900 MeV/c² and a peaking background is located at the range of the PDG value of the η' mass and between 2050 MeV/c² and 2150 MeV/c² of the D mass.

In Figure 29, the offline selection cuts from Table 10 are applied. In this plot the two peaks for the D and D_s signal are clearly visible and at the lower end of the D mass range is a large background contamination (as can be seen in Figure 27 too). This background is distributed nearly constant over the complete range of $m(\eta')$. No further peaking background can be seen in this plot. The signal peaks for D and D_s have a larger width in y direction than in x direction, because in x direction a DTF with a constraint on the η' mass is used. The resolution of the η' mass in y direction is worse, because the detection of a photon in the final state has a bad resolution.

As a conclusion, the BDT cut = -0.8 with a cut on $m(\eta')$ in 1.5σ interval was selected as a final selection. It improves the uncertainty on the yields of the D signal (see Figure 24) and, since the uncertainty of the D_s signal only decreases (see Figure 25), it has the lowest impact on the uncertainty of the D_s signal. The distribution is plotted in in Figure 27.

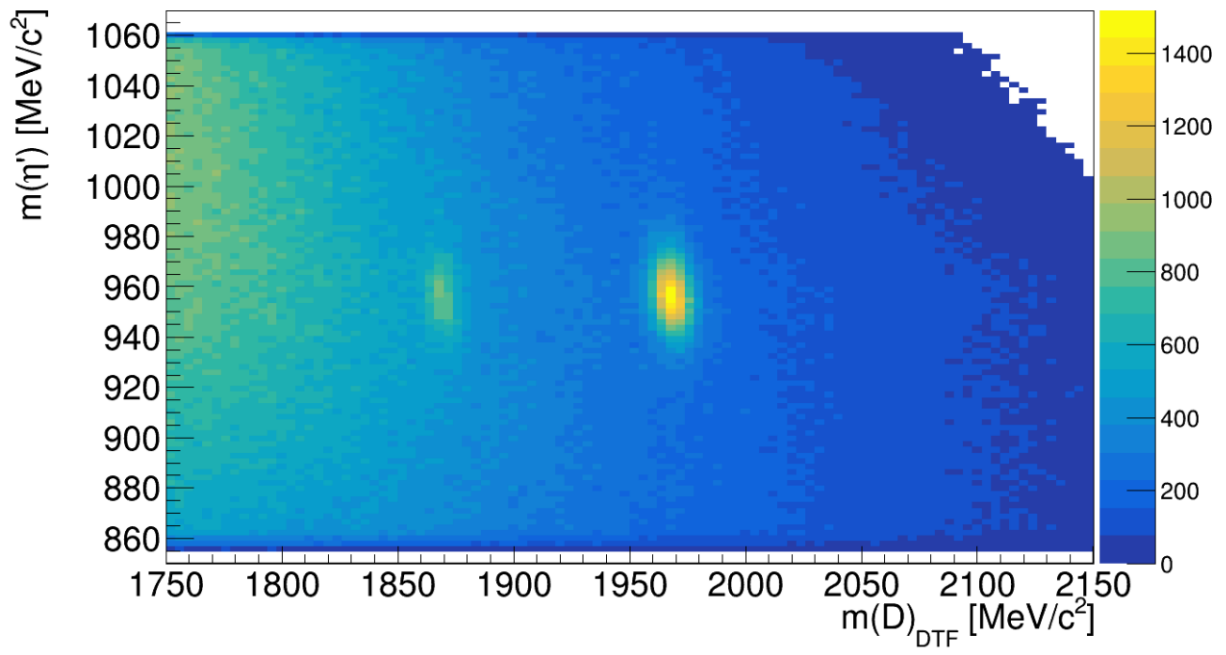


Figure 29: Scatter plot of $m(\eta')$ on the y axis and $m(D)_{DTF}$ on the x axis of the data sample with offline selection cuts applied.

10 Background analysis

In this chapter, possible background components of the decay are investigated and the mechanism for removing these possible background decays is explained.

Possible background sources and their branching ratios are listed in Table 13. Here, the branching ratios are taken from the PDG. The fraction of the BR of a possible background decay and the two decays that are analysed in this thesis has the purpose to get a first idea which background decays are of interest. In Table 13 some branching fractions are in brackets. This notation is used to keep in mind, that these values need to be scaled by the fraction of D to D_s candidates. The branching fractions from Table 13 will change, when applying the selections (offline selection or BDT selection). To take this into account, MC simulations for the individual background decays would be needed to calculate the impact of the selections to the efficiencies of the decays.

A background source is relevant for a decay, if the reconstructed invariant mass with a mass hypothesis peaks around the mass of the D or D_s meson and if the background source has a similar decay topology.

In general, there are two possible types of particle misidentification: Particle misidentification for the charged particle and for the neutral particle.

Table 13: BR of the possible background decays.

Decay	BR of the corresponding decay	BR	
		$BR(D^+ \rightarrow \eta' K^+, \eta' \rightarrow \pi^+ \pi^- \gamma)$	$BR(D_s^+ \rightarrow \eta' K^+, \eta' \rightarrow \pi^+ \pi^- \gamma)$
$D^+ \rightarrow \eta' K^+, \eta' \rightarrow \pi^+ \pi^- \gamma$	$(5.458 \pm 0.008) * 10^{-5}$	1	(0.07)
$D_s^+ \rightarrow \eta' K^+, \eta' \rightarrow \pi^+ \pi^- \gamma$	$(78.175 \pm 0.096) * 10^{-5}$	(14.32)	1
Misidentification of a charged particle			
$D^+ \rightarrow \eta' \pi^+, \eta' \rightarrow \pi^+ \pi^- \gamma$	$(1.466 \pm 0.056) * 10^{-3}$	26.86	(1.88)
$D_s^+ \rightarrow \eta' \pi^+, \eta' \rightarrow \pi^+ \pi^- \gamma$	$(1.1623 \pm 0.0738) * 10^{-2}$	(212.95)	14.87
$D_s^+ \rightarrow \rho^+ \eta', \eta' \rightarrow \pi^+ \pi^- \gamma, \rho^+ \rightarrow \pi^+ \pi^0, \pi^0 \rightarrow \gamma \gamma$	$(1.691 \pm 0.4425) * 10^{-2}$	(309.82)	21.63
$\Lambda_c^+ \rightarrow p^+ \eta', \eta' \rightarrow \pi^+ \pi^- \gamma$	$(1.4455 \pm 0.2655) * 10^{-4}$	2.65	0.18
$D^+ \rightarrow \eta' e^+ \nu_e, \eta' \rightarrow \pi^+ \pi^- \gamma$	$(5.9 \pm 1.18) * 10^{-5}$	1.08	(0.075)
$D_s^+ \rightarrow \eta' e^+ \nu_e, \eta' \rightarrow \pi^+ \pi^- \gamma$	$(2.36 \pm 0.2065) * 10^{-3}$	(43.24)	3.019
$D^+ \rightarrow \eta' \mu^+ \nu_\mu, \eta' \rightarrow \pi^+ \pi^- \gamma$	No value	–	–
$D_s^+ \rightarrow \eta' \mu^+ \nu_\mu, \eta' \rightarrow \pi^+ \pi^- \gamma$	$(0.3245 \pm 0.1475) * 10^{-2}$	(59.45)	4.15
$D^+ \rightarrow \eta' K, \eta' \rightarrow \pi^+ \pi^- \eta, \eta \rightarrow \gamma \gamma$	$(4.073 \pm) * 10^{-5}$	0.746	(0.052)
$D_s^+ \rightarrow \eta' K, \eta' \rightarrow \pi^+ \pi^- \eta, \eta \rightarrow \gamma \gamma$	$(57.8995 \pm) * 10^{-5}$	(10.608)	0.7406
Misidentification of a neutral particle			
$D^+ \rightarrow \phi K^+, \phi \rightarrow \pi^+ \pi^- \pi^0, \pi^0 \rightarrow \gamma \gamma$	$< 0.01805 * 10^{-5}$	< 0.0033	(< 0.00023)
$D_s^+ \rightarrow \phi K^+, \phi \rightarrow \pi^+ \pi^- \pi^0, \pi^0 \rightarrow \gamma \gamma$	$(7.57 \pm 1.74) * 10^{-7}$	(0.014)	0.00097
$D^+ \rightarrow \eta K^+, \eta \rightarrow \pi^+ \pi^- \gamma$	$(0.36875 \pm 0.0472) * 10^{-4}$	0.68	(0.047)
$D_s^+ \rightarrow \eta K^+, \eta \rightarrow \pi^+ \pi^- \gamma$	$(0.51 \pm 0.0236) * 10^{-3}$	(9.34)	0.65

The branching ratios of the intermediate states are listed in Table 14 [10].

Table 14: BR of intermediate decays.

Decay	BR [%]
$\eta' \rightarrow \pi^+ \pi^- \gamma$	29.5 ± 0.4
$\rho^+ \rightarrow \pi^+ \pi^0$	~ 100
$\phi \rightarrow \pi^+ \pi^- \pi^0$	~ 0.87
$\eta' \rightarrow \pi^+ \pi^- \eta$	42.5 ± 0.5
$\eta \rightarrow \gamma \gamma$	51.8 ± 1.8
$\pi^0 \rightarrow \gamma \gamma$	98.823 ± 0.034

10.1 Comparing background decays

To compare the relevance of a possible background decay to the decay channels of interest, it is useful to compare the BR of the background channel to the channels of interest. In Table 13 the ratio of the two corresponding BR's is calculated. This relevance is only possible to calculate, if the MC simulations are available.

To test if a background decay contributes to the selected data events, one can assign a mass hypothesis different to the kaon mass and recalculate the invariant mass of the D meson. The invariant mass distribution with a peak at the D or D_s mass is contributing to the background.

The invariant mass is calculated using the mass of the η' and the momenta that are assigned to the kaon and η' (from the data set). The invariant mass distribution is also cut by the best BDT selection ($m(\eta')$ interval and BDT output).

The invariant mass q is calculated with the mass hypothesis M instead of the K^+ mass and the momenta of the K^+ and η' . It can be computed by:

$$q = \sqrt{\left(\sqrt{p_K^2 + M^2} + \sqrt{p_{\eta'}^2 + m_{\eta'}^2}\right)^2 - \left(p_{x_K} + p_{x_{\eta'}}\right)^2 - \left(p_{y_K} + p_{y_{\eta'}}\right)^2 - \left(p_{z_K} + p_{z_{\eta'}}\right)^2}. \quad (15)$$

The invariant mass distributions q for different mass hypotheses (M) of possible background decays are plotted below. In Figure 30, the mass distributions use information of the data set with pre-cuts applied, the calculated distributions in Figure 31 use the data set with the offline selection cuts applied and the distributions in Figure 32 use the data set with the final selection cuts applied. The mass distributions can be split into two categories, one category including

the decays $D_{(s)} \rightarrow \eta K$, $D_{(s)} \rightarrow \eta' e$, $D_{(s)} \rightarrow \eta' \mu$ and $D_{(s)} \rightarrow \eta' \pi$ is located in a mass range between 1000 to 2100 MeV/c^2 and the second category with the decays $\Lambda_c \rightarrow \eta' p$, $D_{(s)} \rightarrow \pi^+ \pi^- \eta K$ and $D_s \rightarrow \eta' \rho^+$ is located between 1900 to 3500 MeV/c^2 .

In Figure 30, peaks around the D and D_s mass are visible for the decays, where a e, μ or π is misidentified as a K . This is an indicator for a contribution of these decays in the data sample with only pre-cuts applied.

After the offline selection, the above mentioned peaks vanished and the decay $D_{(s)} \rightarrow \pi^+ \pi^- \eta K$ is reduced between 1900 and 2100 MeV/c^2 . This can be explained by the cut $m(\pi^+ \pi^- K) < 1825 \text{ MeV}/c^2$ (from section 9.2), because the decay $\eta \rightarrow \gamma \gamma$ produces one photon more than the η' decay of interest.

After applying the final selection cuts, the mass distributions of the decays $D_{(s)} \rightarrow \eta' e$, $D_{(s)} \rightarrow \eta' \mu$ and $D_{(s)} \rightarrow \eta' \pi$ form small peaks around the D_s mass, because the distribution is reduced between 1890 and 1940 MeV/c^2 (the range which is set by the peaks of the D and D_s peaks).

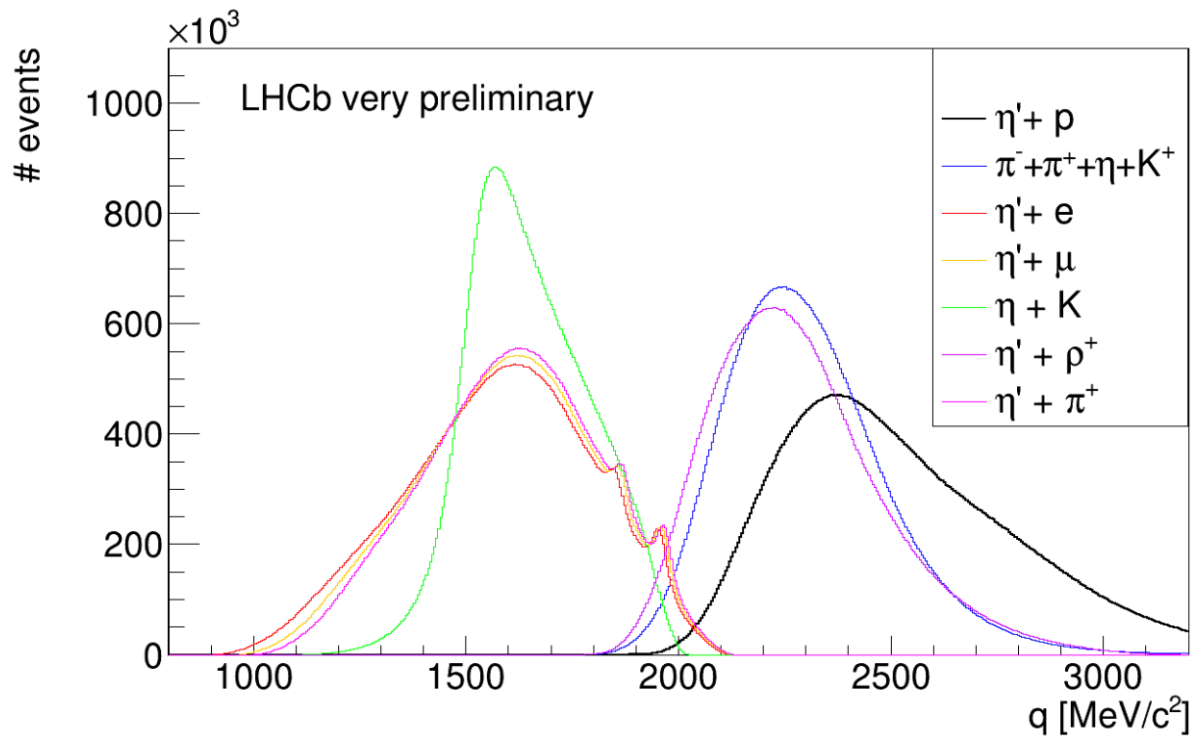


Figure 30: Different invariant masses of possible background decay channels with the data set where only pre-cuts are applied.

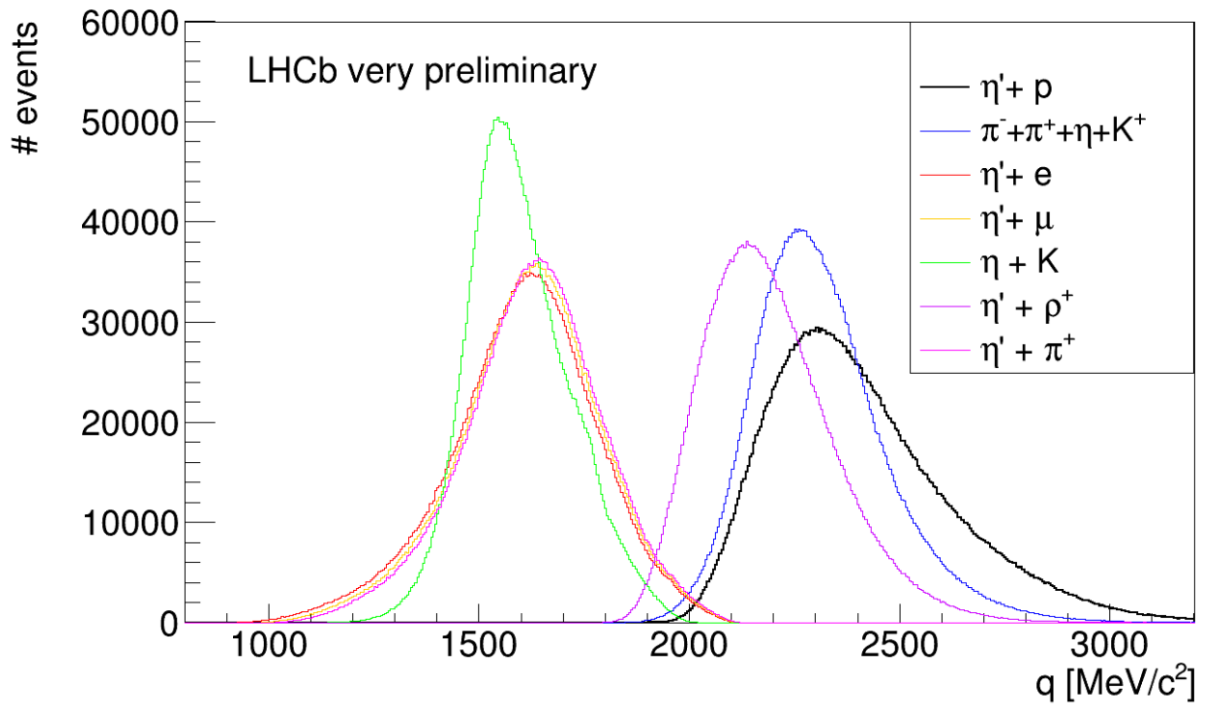


Figure 31: Different invariant masses of possible background decay channels with the data set where the offline selection cuts from section 9.2 are applied.

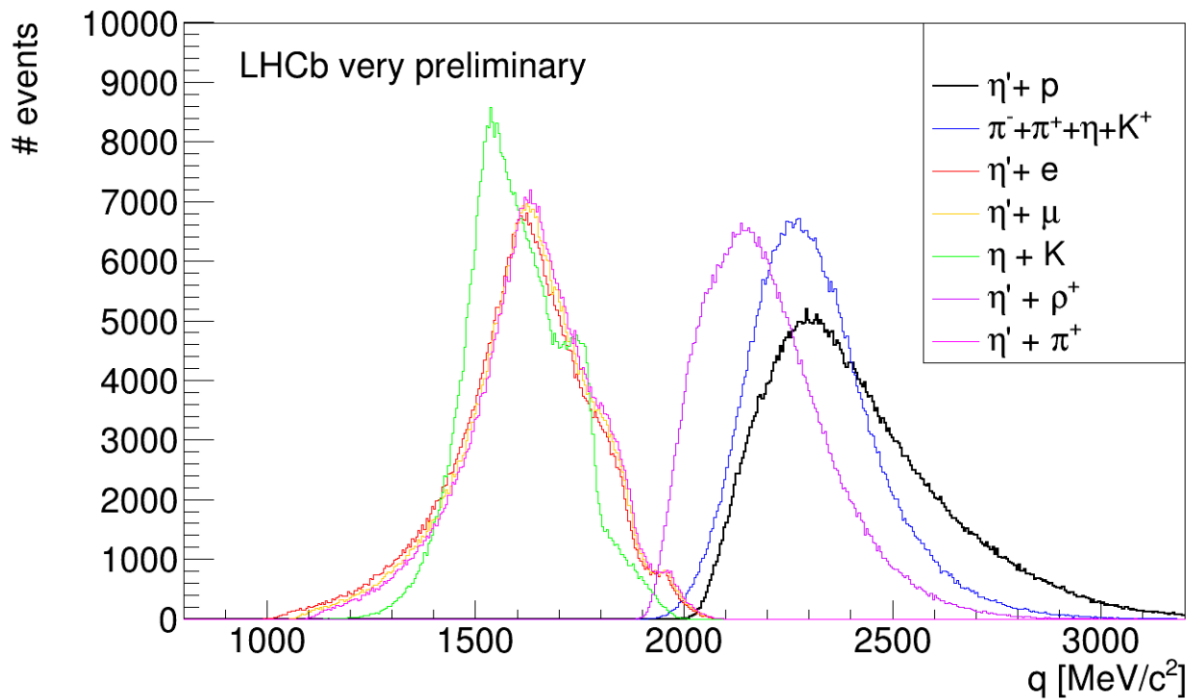


Figure 32: Different invariant masses of possible background decay channels with the data set where the offline selections cuts from section 9.2, a cut on BDT output > -0.8 and a cut on $m(\eta') \in 1.5\sigma$ interval are applied (final selection).

10.2 Technique to remove background decays

The invariant mass distributions is calculated with different DLL cuts applied on the data. For the pion mass hypothesis $M = m(\pi^+)$ the $DLL_{K\pi}$ of the kaon is used. The analysis is performed to this point without this $DLL_{K\pi}$ cut (from section 9.2). Then, a scan for the different cuts on the $DLL_{K\pi}$ of the kaon is performed. To find the best $DLL_{K\pi}$ cut, one wants to cut on the value, where the largest peaks around the $D_{(s)}$ mass are visible, and the inverse cut shows no peaks in these mass regions. When applying the cut where no peaks are visible, the background contamination in the background data is reduced. The cut $DLL_{K\pi} > 8$ is chosen. This DLL cut needs to be applied in the offline selection (before the BDT), so that the classifier can better separate background from signal.

As one can see in Figure 33, it is not possible to remove the background decay completely. After the final selection (BDT cut and cut on $m(\eta')$ interval) peaks around the D and D_s mass are remaining with a higher cut on $DLL_{K\pi} < 10$.

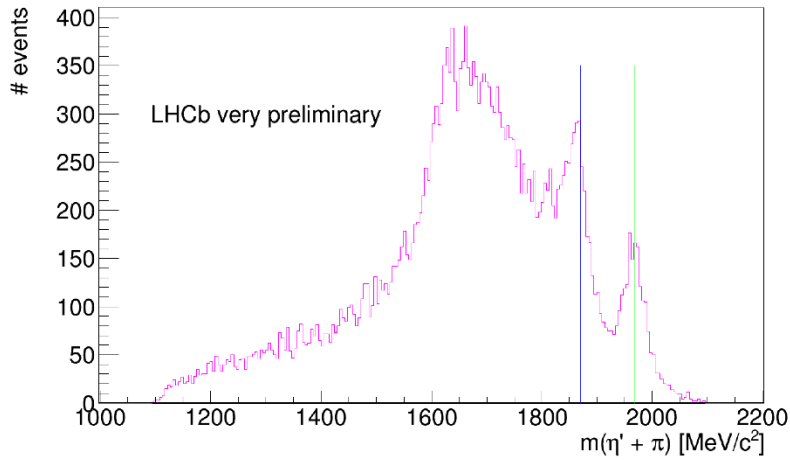


Figure 33: Invariant mass distribution of the pion mass hypothesis with final selection and with the cut $DLL_{K\pi} < 10$. Vertical lines indicating the mass of the D meson (blue) and D_s meson (green).

To reduce all relevant background decays from Table 13, the same procedure as for the pion mass hypothesis is repeated for electron, muon, and proton mass hypothesis. For these decays the DLL_{xy} from section 6 is used. For the $e (\mu) \rightarrow K$ mis-id there is a background contribution which has a little offset to the left and is largest for $DLL_{eK} (DLL_{\mu K}) > -20$ (see Figure 34).

As a conclusion of the background analysis, one has to mention that the largest background contribution after the selection and the BDT cut are the decays $D_{(s)} \rightarrow \eta' e$ and $D_{(s)} \rightarrow \eta' \mu$. Cuts on the mentioned DLL cut for the decay $D_{(s)} \rightarrow \eta' e$ are applied. However, this cut did not improve the resolution of the two signal peaks and did not change the shape of the invariant mass distribution of the D meson, so it was decided to not apply this cut in the final analysis.

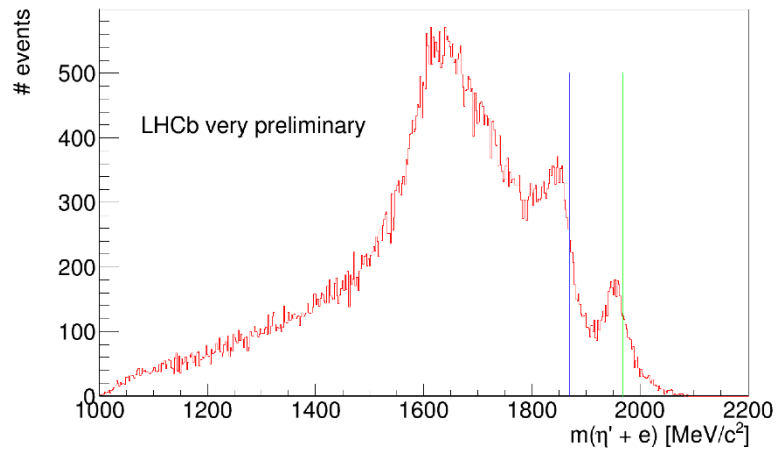


Figure 34: Invariant mass distribution with the electron mass hypothesis and with the cut $DLL_{e\pi} > -20$. Vertical lines indicating the mass of the D meson (blue) and D_s meson (green).

11 Fit routine

After the final selection and the background analysis, the $m(D)_{DTF}$ is fitted in the range [1780, 2150] MeV/c².

The uncertainty of each bin in the histograms of the mass distribution is described by a Poisson distribution. Here, a bin size of 2 MeV/c² is chosen.

For the final fit, several combinations of fit functions for the joint probability density function (pdf) are tried to model the data with the best precision available. For the different components the following possible distributions are tried:

$D^+ \rightarrow \eta' K^+$ signal: Gaussian or Johnson SU function,

$D_s^+ \rightarrow \eta' K^+$ signal: Gaussian or Johnson SU function,

Combinatorial background: Chebyshev polynomial (third or second order)

The pdf model is fitted with the RooFit implementation in Root and uses Iminuit for a least square fit.

A candidate for the signal component is the Johnson SU function which is defined as

$$Johnson\ SU(x) = \frac{\delta}{\lambda \sqrt{2\pi}} \frac{1}{\sqrt{1 + \left(\frac{x-\mu}{\lambda}\right)^2}} \exp\left(-\frac{1}{2}\left(\gamma + \delta \sinh^{-1}\left(\frac{x-\mu}{\lambda}\right)\right)^2\right).$$

Here μ defines the mean of the Gaussian component and λ the width, γ the location of the tail to the left/right and δ the strength of the Gaussian [37, 38].

The Chebyshev polynomial of the first kind is of the form:

$$P(x) = 1 + a_0 T_1(x) + a_1 T_2(x) + a_2 T_3(x)$$

with $T_n(\cos(\theta)) = \cos(n\theta)$ [39]. This is used instead of a classical polynomial because the Chebyshev polynomials are orthogonal, so varying one of the coefficients a_i does not influence the others. This helps to find a more stable solution in the fitting process. The stability of the fit is important, because it is one of the contributions of the systematic uncertainty.

A pdf with a third order Chebyshev polynomial for the combinatorial background, a Gaussian for the signal of the D meson and a Johnson SU function for the D_s signal describes the data best and has the smallest χ^2 of the fit. The final fit can be seen in Figure 35 and the fit parameters with their uncertainties are listed in Appendix G. The residuals are mostly in a range of 2σ , but with some systematic under and overshoot between the D and D_s signal peak as well as in the range above the D_s signal around 2080 MeV/c^2 .

The number of the $D_{(s)}$ signals candidates of the final fit are

$$N(D^+ \rightarrow \eta' K^+) = 13890 \pm 266,$$

$$N(D_s^+ \rightarrow \eta' K^+) = 51342 \pm 352.$$

They result in an estimation of the statistical uncertainty of the CP asymmetry of the two decays using Equation (14) from section 5:

$$\sigma_{stat}(A_{CP}(D^+ \rightarrow \eta' K^+)) = 1.9 \%,$$

$$\sigma_{stat}(A_{CP}(D_s^+ \rightarrow \eta' K^+)) = 0.7 \%.$$

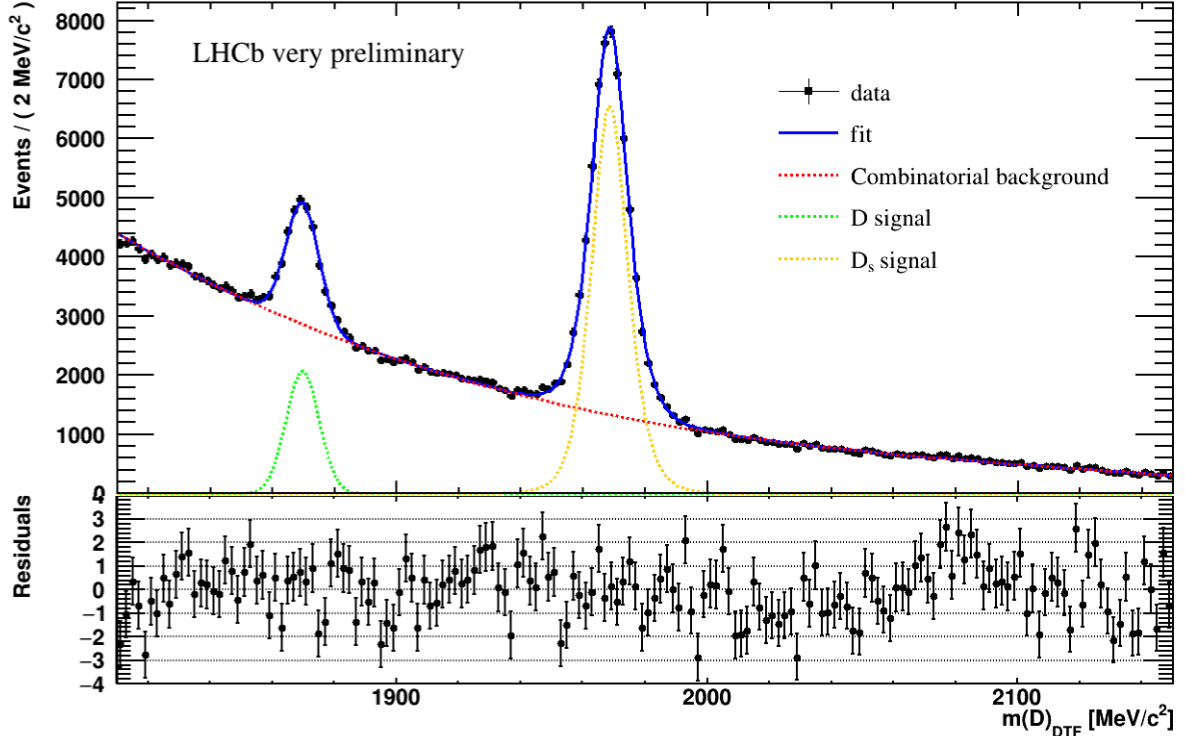


Figure 35: Fit of $m(D)_{DTF}$ after the final selection and background analysis. Total fit pdf (blue) consisting of the gaussian model for the D signal (green), the Johnson model for the D_s signal (orange) and the combinatorial background component (red).

12 Conclusion

This thesis reports an optimisation of the selection of $D^+ \rightarrow \eta' K^+$ and $D_s^+ \rightarrow \eta' K^+$ decay channels with the aim to gain the best sensitivity for the CP asymmetry measurements in these decays by reconstructing $\eta' \rightarrow \pi^+ \pi^- \gamma$ exploiting 5.7 fb^{-1} of Run2 data of the LHCb experiment at a centre-of-mass energy of $\sqrt{s} = 13 \text{ TeV}$. First, it was necessary to reduce the background by an offline selection and to remove combinatorial background using a BDT. For further studies of the two decay chains of interest, a background analysis was performed. The final values were obtained by fitting the reconstructed D and D_s signals. The following estimates for the expected statistical uncertainty are found:

$$\sigma_{stat}(A_{CP}(D^+ \rightarrow \eta' K^+)) = 1.9 \%,$$

$$\sigma_{stat}(A_{CP}(D_s^+ \rightarrow \eta' K^+)) = 0.7 \%.$$

Previously there was only one measurement for the CP asymmetry of the SCS channel:

$$A_{CP}(D_s^+ \rightarrow \eta' K^+) = (6 \pm 18.9 \pm 0.9)\%,$$

where the first uncertainty is statistical and the second one systematic [7]. For the $D^+ \rightarrow \eta' K^+$ channel, there was until now no measurement due to lack of statistics [7]. This thesis demonstrates that with the larger statistics at the LHCb, it is possible to reduce the statistical uncertainty $\sigma_{stat}(A_{CP}(D_s^+ \rightarrow \eta' K^+))$ by a factor of 27.

To improve the analysis, a more detailed investigation of the behaviour of the problem with the BDT cut for the D_s signal is needed. Including partially reconstructed background components in the fit can improve the resolution of the signal distributions.

The next steps for a measurement of the CP asymmetries in these decays is the evaluation of the systematic uncertainties, the analysis of a control channel and the calculation of the central A_{CP} value.

Appendix

A Trigger lines

The trigger lines used in this analysis are shown in Table 15 for the different Trigger levels.

Table 15: L0, HLT1 and HLT2 trigger lines.

Trigger level	Trigger line
L0	eta_L0HadronDecision_TOS or D_L0HadronDecision_TIS or D_L0PhotonDecision_TIS or D_L0MuonDecision_TIS or D_L0DiMuonDecision_TIS or D_L0ElectronDecision_TIS
HLT1	eta_Hlt1TwoTrackMVADecision_TOS or eta_Hlt1TrackMVADecision_TOS
HLT2	Hlt2CharmHadDp2EtapKp_Etap2PimPipGDecision

B Offline selection cuts on $m(\pi^+\pi^-)$ and $m(\pi^+\pi^-K)$

The invariant mass distribution of the two daughter pions of the η' is plotted in Figure 36 from the data sample with pre-cuts applied. The cut $m(\pi^+\pi^-) > 600 \text{ MeV}/c^2$ is sufficient to reduce background, which is visible smaller masses. The reason for this cut is, that the η' decays via a $\rho^0(770)$ resonance. This can be seen in the plot, since the distribution peaks around $770 \text{ MeV}/c^2$.

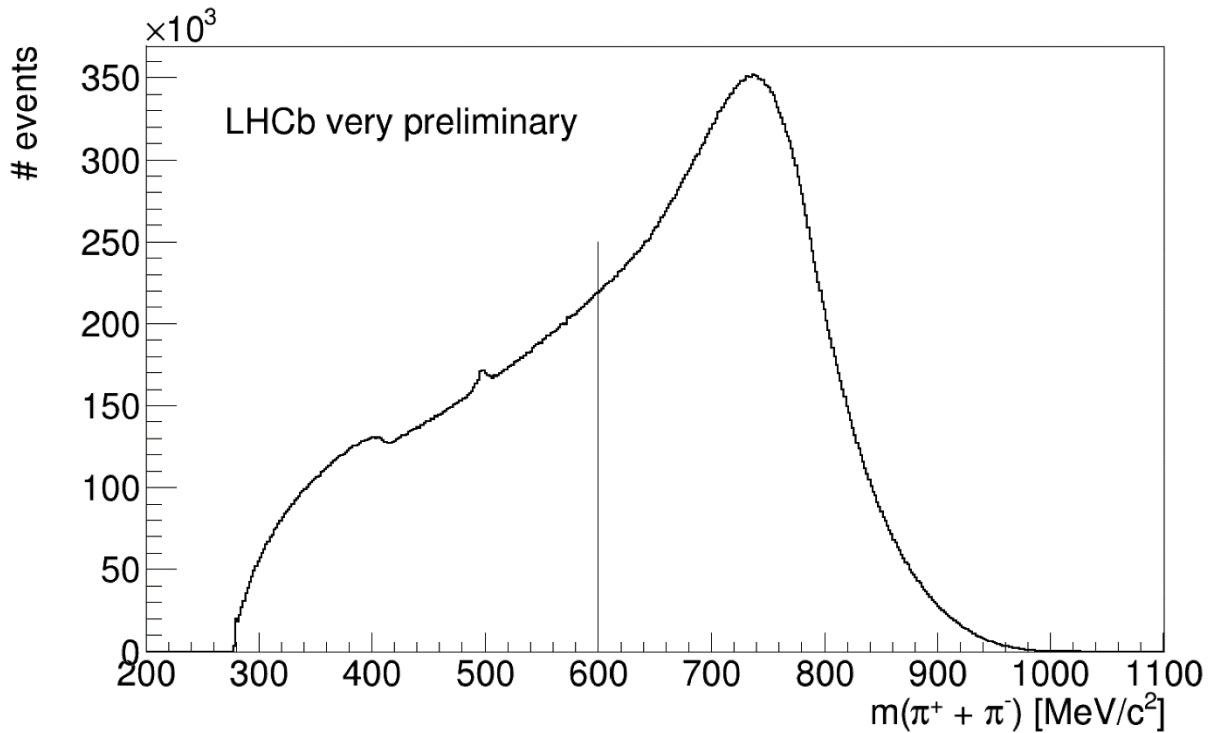


Figure 36: $m(\pi^+\pi^-)$ is plotted with the cut from the offline selection (vertical line) at $m(\pi^+\pi^-) = 600 [\text{MeV}/c^2]$.

The invariant mass distribution of the two daughter pions of the η' and the kaon is plotted in Figure 37 from the data sample only with pre-cuts applied. The cut $m(\pi^+\pi^-K) < 1825 \text{ MeV}/c^2$ reduces background where a photon is accidentally included in the decay. The reason for this cut is the comparison of the left and right tail of the mass distribution, because the right tail is higher and short.

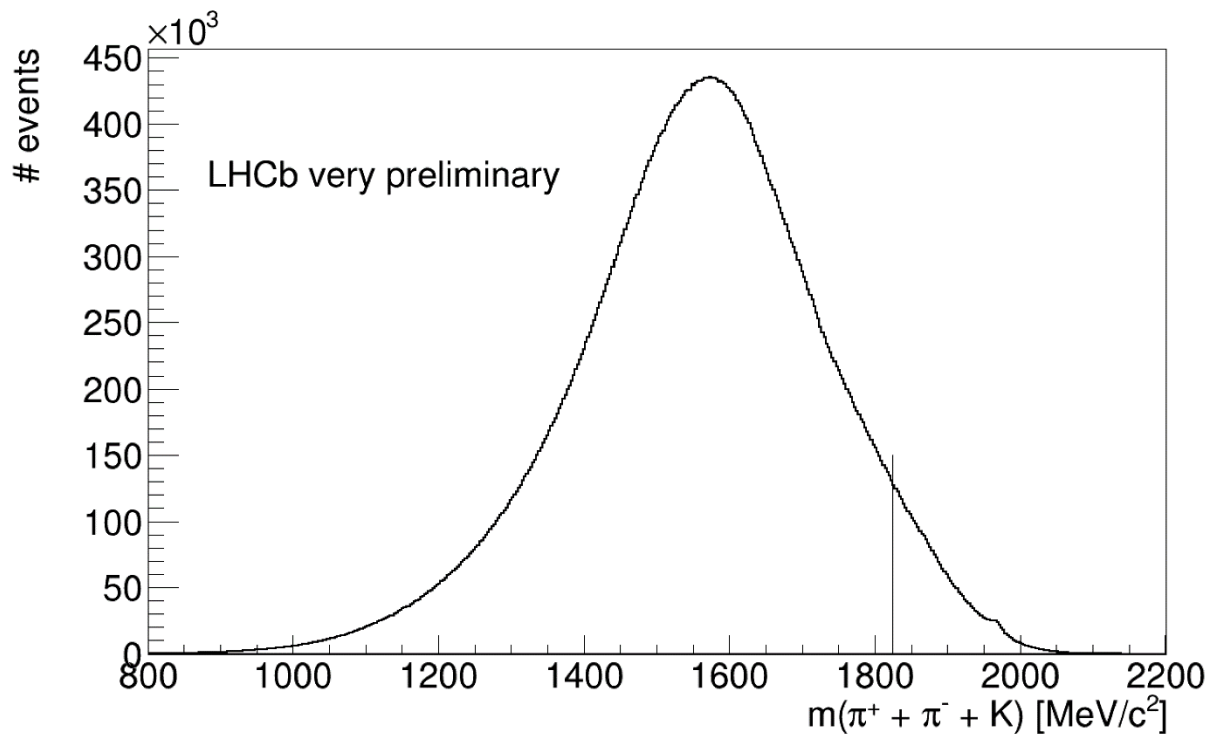


Figure 37: $m(\pi^+\pi^-K)$ is plotted with the cut from the offline selection (vertical line) at $m(\pi^+\pi^-K) = 1825$ [MeV/c²].

C $m(\eta')$ fit

The fit for the mean of the $m(\eta')$ is performed by fitting a gaussian to the reconstructed mass of the η' after the offline selection cuts are applied.

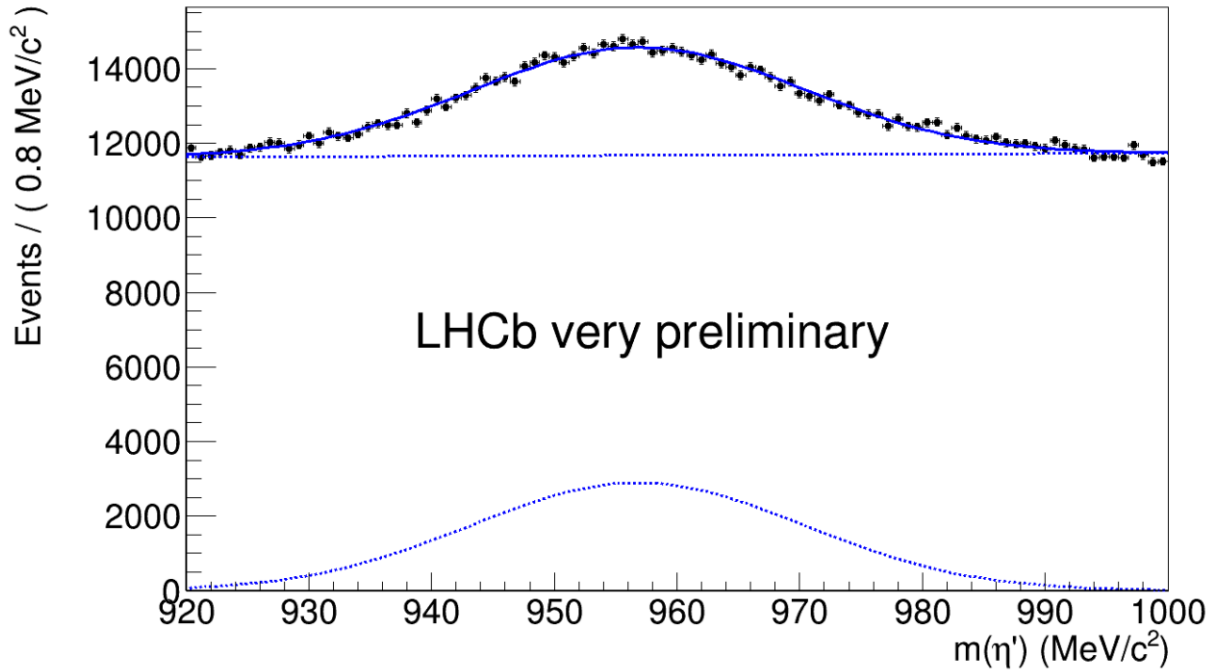


Figure 38: η' mass fit.

In Figure 38 this fit is plotted. The mean is at $957 \text{ MeV}/c^2$ and $\sigma \approx 13 \text{ MeV}/c^2$. The three intervals for the 1 , 1.5 , 2σ regions around the mean correspond to:

$$1\sigma \text{ interval} = [944, 970] \text{ MeV}/c^2$$

$$1.5\sigma \text{ interval} = [937.5, 976.5] \text{ MeV}/c^2$$

$$2\sigma \text{ interval} = [931, 983] \text{ MeV}/c^2$$

$$4\sigma \text{ interval} = [905, 1009] \text{ MeV}/c^2$$

D BDT Analysis

Here the input variables for the BDT are plotted. For each variable the signal and background distribution is plotted normalized in the same plot (see Figure 39 to Figure 46).

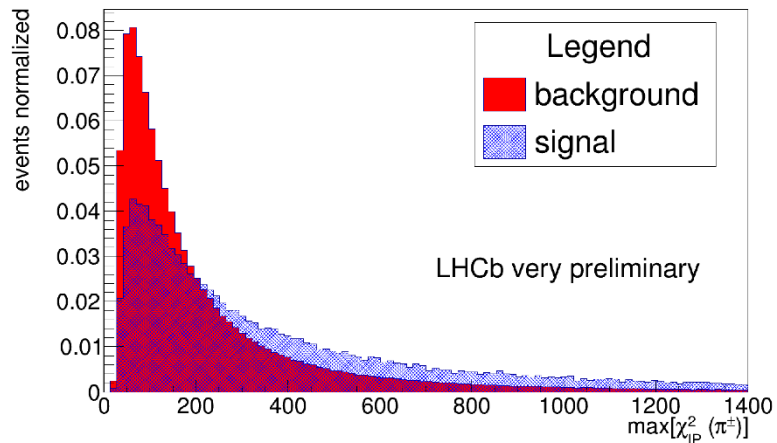


Figure 39: Maximum of χ^2_p for the daughter pions of the η' . Plots normalized for signal (blue) and background (red).

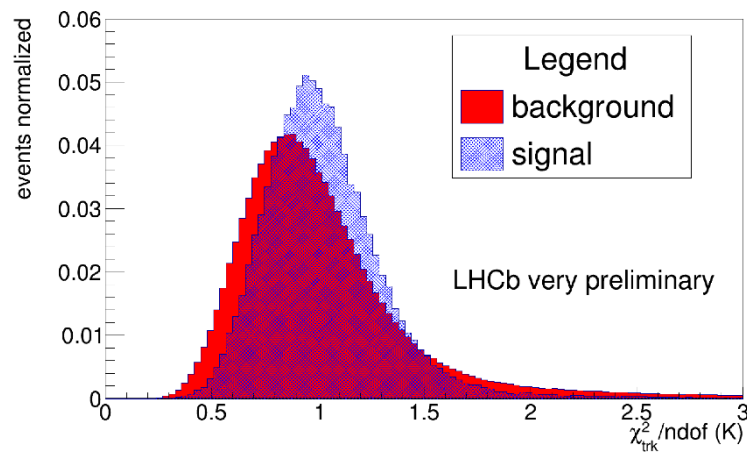


Figure 40: $\chi^2_{\text{trk}}/\text{ndof}$ of the kaon. Plots normalized for signal (blue) and background (red).

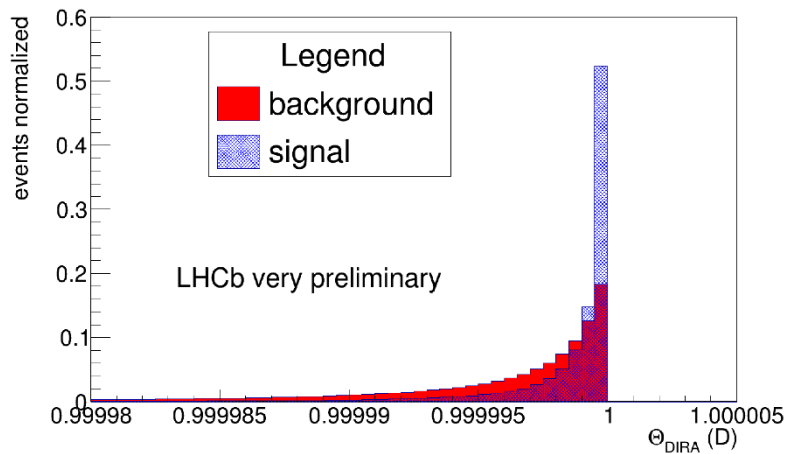


Figure 41: θ_{DIRA} of the D meson. Plots normalized for signal (blue) and background (red).

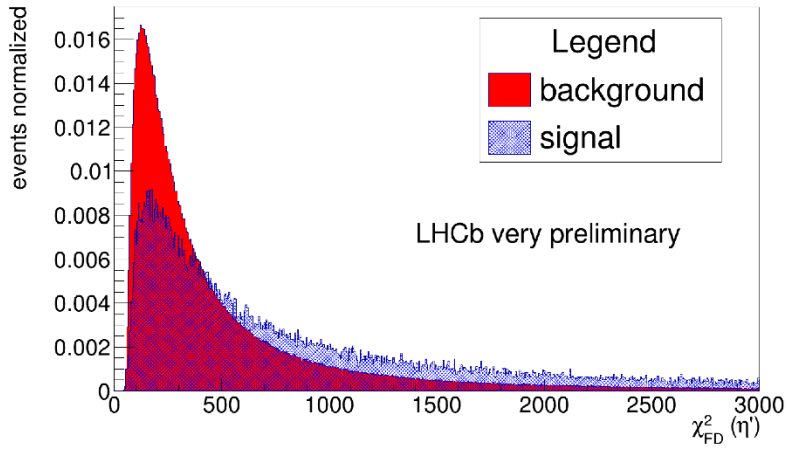


Figure 42: χ^2_{FD} of the η' . Plots normalized for signal (blue) and background (red).

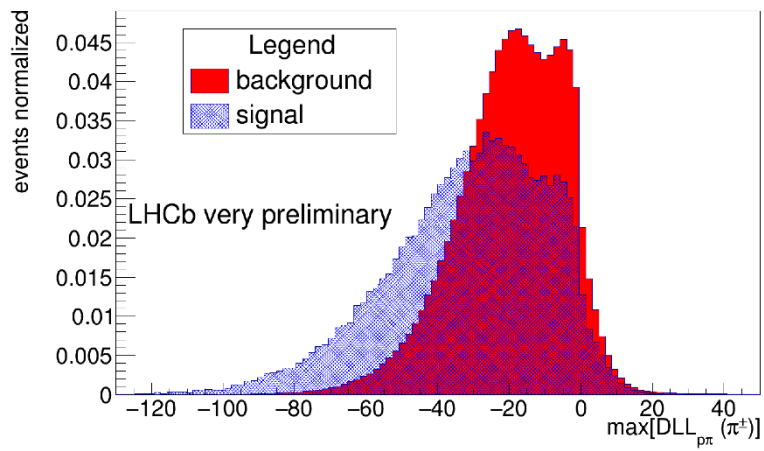


Figure 43: Maximum of $DLL_{p\pi}$ of the daughter pions of the η' . Plots normalized for signal (blue) and background (red).

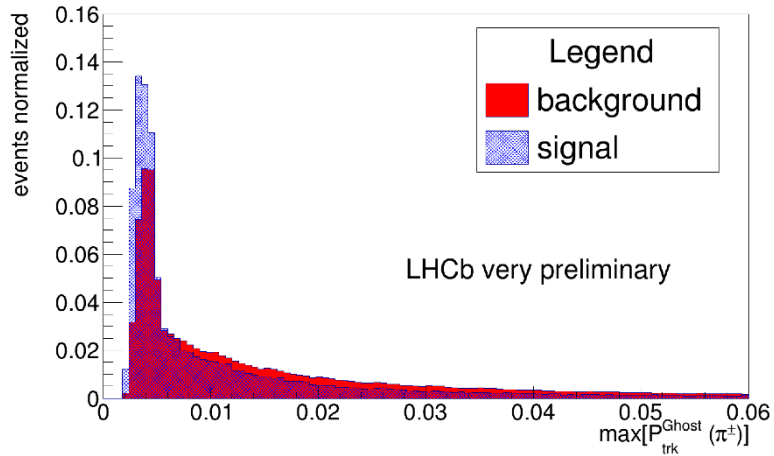


Figure 44: Maximum of P_{trk}^{ghost} of the daughter pions of the η' . Plots normalized for signal (blue) and background (red).

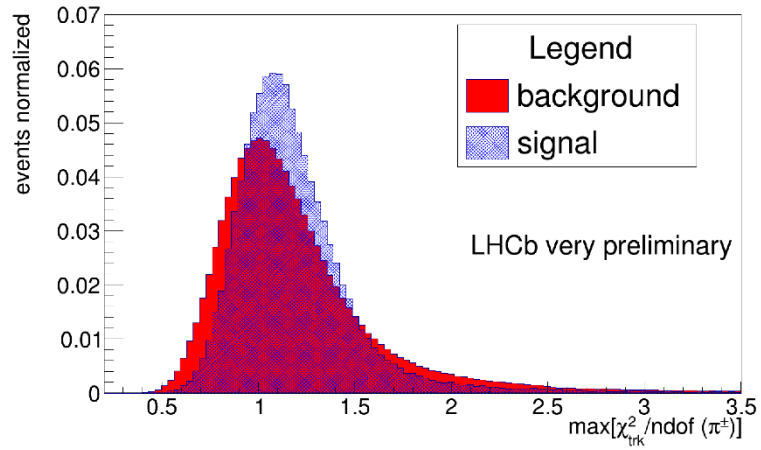


Figure 45: Maximum of $\chi^2_{\text{trk}}/\text{ndof}$ of the daughter pions of the η' . Plots normalized for signal (blue) and background (red).

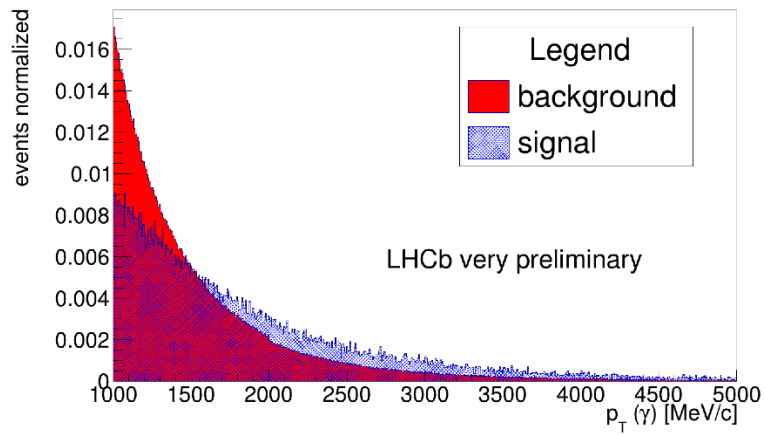


Figure 46: Transverse momentum of the γ . Plots normalized for signal (blue) and background (red).

E Scan for best BDT parameters

For the scan one parameter is allowed to float, while setting the other parameters fixed. It was started with the number of trees in the BDT (Table 16).

Table 16: Scan for the BDT parameters (I): Varying the number of trees in the BDT (NTrees).

NTrees	500	600	400	300
MaxDepth	2	2	2	2
MinNodeSize	5%	5%	5%	5%
BoostType	<i>Grad</i>	<i>Grad</i>	<i>Grad</i>	<i>Grad</i>
Integrated ROC value	0.850	0.850	0.850	0.849
p-value for signal (background)	0.01 (0.274)	0.005 (0.144)	0.011 (0.359)	0.001 (0.438)

The integrated ROC-curve value stays the same when varying the number of trees in the BDT. For 400 trees, the p-value is the highest for signal and background. In the next step the maximal depth of one decision trees is changed (Table 17).

Table 17: Scan for the BDT parameters (II): Varying the maximal depth of one decision tree (MaxDepth).

NTrees	400	400
MaxDepth	3	4
MinNodeSize	5%	5%
BoostType	<i>Grad</i>	<i>Grad</i>
Integrated ROC value	0.854	0.853
p-value for signal (background)	0 (0)	0 (0)

A decision tree with more cuts has a better ROC value, but the p-value is zero so they can not be used. The minimal size of a node was changed to 4 and 6 percent (Table 18).

Table 18: Scan for the BDT parameters (III): Varying the minimal size a leaf must contain to be classified as signal or background (MinNodeSize).

NTrees	400	400
MaxDepth	2	2
MinNodeSize	4%	6%
BoostType	<i>Grad</i>	<i>Grad</i>
Integrated ROC value	0.853	0.850
p-value for signal (background)	0 (0.115)	0.008 (0.338)

The BDT with 4% MinNodeSize has a p-value of 0 for the signal and the one with 6% has lower p-values than the BDT in red. It was chosen to use the BDT in red, because it has the highest p-values and a high enough area under the ROC curve.

At a last step the type of boosting was changed to adaptive boosting, instead of gradient boosting (Table 19).

Table 19: Scan for the BDT parameters (IV): Changing the BoostType to AdaBoost.

NTrees	400
MaxDepth	2
MinNodeSize	5%
BoostType	<i>AdaBoost</i>
Integrated ROC value	0.849
p-value for signal (background)	0.024 (0.807)

The ROC curve for the selected BDT (in red) is plotted in Figure 47.

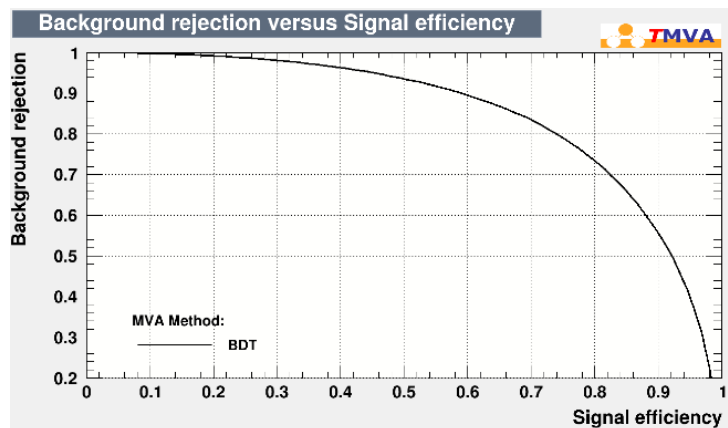


Figure 47: Background rejection against signal efficiency for the selected BDT.

F Determine the BDT cut

The tables for the BDT cut scan for the three $m(\eta')$: 1.5σ , 1σ and 2σ interval are given in Table 20, Table 21, Table 22.

Table 20: Signal yields and there uncertainty for the D and D_s channel (for 1.5σ η' mass interval) for different BDT cuts.

BDT output & $m(\eta') \in$ [937.5, 976.5] MeV/c^2	$N(D)$ [events]	$N(D_s)$ [events]	$\sigma(D)$ [%]	$\sigma(D_s)$ [%]
> -1	14970 ± 345	56076 ± 359	2.30	0.64
> -0.9	14603 ± 327	55892 ± 346	2.24	0.62
> -0.8	13674 ± 296	48506 ± 316	2.16	0.65
> -0.7	12904 ± 272	43309 ± 291	2.11	0.67
> -0.6	11896 ± 247	38590 ± 269	2.08	0.70
> -0.5	10839 ± 226	34329 ± 250	2.09	0.73
> -0.4	9870 ± 206	30447 ± 233	2.09	0.77
> -0.3	9021 ± 191	26697 ± 215	2.12	0.81
> -0.2	8071 ± 175	23291 ± 199	2.17	0.85
> -0.1	7171 ± 160	20233 ± 184	2.23	0.91
> 0	6320 ± 146	17173 ± 168	2.31	0.98
> 0.1	5530 ± 132	14435 ± 153	2.39	1.06
> 0.2	4735 ± 118	11894 ± 138	2.49	1.16
> 0.3	4019 ± 105	9548 ± 123	2.61	1.29
> 0.4	3213 ± 91	7472 ± 108	2.83	1.45
> 0.5	2513 ± 78	5426 ± 91	3.10	1.68
> 0.6	1892 ± 66	3770 ± 75	3.49	1.99
> 0.7	1260 ± 50	2381 ± 59	3.97	2.48
> 0.8	706 ± 36	1258 ± 43	5.10	3.42
> 0.9	270 ± 20	370 ± 25	7.41	6.76

Table 21: Signal yields and the uncertainty for the D and D_s channel (for 1σ η' mass interval) for different BDT cuts.

BDT output & $m(\eta') \in$ [944, 970] MeV/c^2	$N(D)$ [events]	$N(D_s)$ [events]	$\sigma(D)$ [%]	$\sigma(D_s)$ [%]
> -1	11596 ± 273	45033 ± 305	2.35	0.68
> -0.9	11307 ± 263	43285 ± 295	2.33	0.68
> -0.8	10595 ± 239	38903 ± 271	2.26	0.70
> -0.7	10128 ± 223	34734 ± 250	2.20	0.72
> -0.6	9338 ± 204	30910 ± 232	2.18	0.75
> -0.5	8471 ± 186	27497 ± 216	2.20	0.79
> -0.4	7784 ± 171	24380 ± 200	2.20	0.82
> -0.3	7125 ± 129	21367 ± 185	2.23	0.87
> -0.2	6448 ± 146	18643 ± 171	2.26	0.92
> -0.1	5753 ± 133	16177 ± 159	2.31	0.99
> 0	5116 ± 122	13735 ± 145	2.38	1.06
> 0.1	4482 ± 110	11544 ± 132	2.45	1.14
> 0.2	3816 ± 99	9507 ± 119	2.59	1.25
> 0.3	3217 ± 88	7648 ± 107	2.74	1.40
> 0.4	2556 ± 76	5970 ± 93	2.97	1.56
> 0.5	1968 ± 64	4357 ± 79	3.25	1.81
> 0.6	1470 ± 53	3000 ± 65	3.61	2.17
> 0.7	976 ± 41	1902 ± 51	4.20	2.68
> 0.8	533 ± 29	997 ± 38	5.44	3.81

No values for a BDT output > 0.9 are given, since the fit did not converge. The reason could be, that too few events are remaining after this BDT cut.

Table 22: Signal yields and there uncertainty for the D and D_s channel (for 2σ η' mass interval) for different BDT cuts.

BDT output & $m(\eta') \in$ [931, 983] MeV/c^2	$N(D)$ [events]	$N(D_s)$ [events]	$\sigma(D)$ [%]	$\sigma(D_s)$ [%]
> -1	16650 ± 388	61520 ± 398	2.33	0.65
> -0.9	16462 ± 374	58963 ± 381	2.27	0.65
> -0.8	15375 ± 343	53128 ± 348	2.23	0.66
> -0.7	14439 ± 308	47441 ± 320	2.13	0.67
> -0.6	13219 ± 279	42240 ± 295	2.11	0.70
> -0.5	12008 ± 255	37662 ± 274	2.12	0.73
> -0.4	10953 ± 233	33352 ± 254	2.13	0.76
> -0.3	9985 ± 215	29225 ± 235	2.15	0.80
> -0.2	8916 ± 196	25516 ± 217	2.20	0.85
> -0.1	7892 ± 178	22111 ± 200	2.26	0.90
> 0	6971 ± 163	18770 ± 183	2.34	0.97
> 0.1	6092 ± 147	15812 ± 166	2.41	1.05
> 0.2	5209 ± 131	13059 ± 149	2.51	1.14
> 0.3	4374 ± 115	10480 ± 133	2.63	1.27
> 0.4	3523 ± 100	8176 ± 116	2.84	1.42
> 0.5	2762 ± 87	5931 ± 98	3.15	1.65
> 0.6	2060 ± 73	4140 ± 81	3.54	1.96
> 0.7	1370 ± 63	2612 ± 63	4.60	2.41
> 0.8	765 ± 40	1389 ± 47	5.23	3.38
> 0.9	290 ± 21	414 ± 27	7.24	6.52

G Fit parameter

The fit parameters and their uncertainties of the final fit are listed in Table 23.

Table 23: Fit values of the pdf of the final fit.

pdf component	fit parameter	value
<i>Chebyshev polynomial</i>	a_0	-1.0841 ± 0.0027
	a_1	0.3168 ± 0.0033
	a_2	-0.0611 ± 0.0027
<i>Johnson SU</i>	δ	1.78 ± 0.08
	γ	-0.08 ± 0.04
	λ	$(11.1 \pm 0.5) \text{ MeV}/c^2$
	μ	$(1968.00 \pm 0.23) \text{ MeV}/c^2$
<i>Gaussian</i>	μ	$(1869.54 \pm 0.11) \text{ MeV}/c^2$
	σ	$(5.37 \pm 0.11) \text{ MeV}/c^2$
<i>Combinatorial background</i>	N_{bkg}	271413 ± 650
<i>D signal</i>	$N(D^+ \rightarrow \eta' K^+)$	13890 ± 266
<i>D_s signal</i>	$N(D_s^+ \rightarrow \eta' K^+)$	51342 ± 352

An interesting cross check is to compare the mean values of the signal components with the mass values from the PDG. For the $m(D)$ one can calculate a sigma deviation of $\sigma_{m(D)} = \frac{1869.54 - 1869.66}{\sqrt{0.05^2 + 0.11^2}} = 0.99\sigma$ and for the $m(D_s)$ a sigma deviation of $\sigma_{m(D_s)} = \frac{1968.00 - 1968.35}{\sqrt{0.07^2 + 0.23^2}} = 1.46\sigma$ by using the uncertainty of the fit as the uncertainty of the mean. Since the deviations are in a two sigma region, the fit seems compatible.

Bibliography

- [1] W. Hulsbergen, Decay Chain Fitting with a Kalman Filter, [arXiv:physics/0503191v1](https://arxiv.org/abs/physics/0503191v1) (2005)
- [2] Lukas Calefice, Standalone track reconstruction on GPUs in the first stage of the upgraded LHCb trigger system & Preparations for measurements with strange hadrons in Run 3, 13.12.2022
- [3] Emma Hicks, A measurement of $\sigma(Z \rightarrow \mu\mu)$ using the LHCb detector at CERN, 09.2012
- [4] Giulia Tuci, Searching for confirmation of charm CP violation in K_S^0 final states at LHCb, 31.12.2020, CERN-THESIS-2020-325
- [5] Sather, Eric. "[The Mystery of the Matter Asymmetry](#)" (PDF). *Vanderbilt University*. Retrieved 03.04.2018
- [6] LHCb collaboration, Observation of CP violation in charm decays, [arXiv:1903.08726](https://arxiv.org/abs/1903.08726)
- [7] Cleo Collaboration, Measurements of D Meson Decays to Two Pseudoscalar Mesons, 17.06.2009, [arXiv:0906.3198v1](https://arxiv.org/abs/0906.3198v1)
- [8] Hai-Yang Cheng, Cheng-Wei Chiang, Direct CP violation in two-body hadronic charmed meson decays, 22.02.2012
- [9] Wikipedia, [File:Standard Model of Elementary Particles.svg - Wikipedia](#)
- [10] **R.L. Workman *et al.* (Particle Data Group), *Prog. Theor. Exp. Phys.* **2022**, 083C01 (2022) and 2023 update**
- [11] Mark Thomson, Modern particle physics, Cambridge, 2013
- [12] ATLAS collaboration, Observation of a new particle in the search for the Standard Model Higgs boson with the ATLAS detector at the LHC, 31.08.2012
- [13] Lehnert, R. CPT Symmetry and Its Violation. *Symmetry* **2016**, 8, 114. <https://doi.org/10.3390/sym8110114>
- [14] A. Ceccucci (CERN), Z. Ligeti (LBNL) and Y. Sakai (KEK), rpp2020-rev-ckm-matrix, 03.2020
- [15] "CERN Document Server - Multimedia and Outreach", CERN-AC-9906026, <http://cdsweb.cern.ch/record/40525>, (1999)
- [16] LHCb collaboration, $b\bar{b}$ production angle plots, https://lhcb.web.cern.ch/lhcb/speakersbureau/html/bb_ProductionAngles.html{https://lhcb.web.cern.ch/lhcb/speakersbureau/html/bb_ProductionAngles.html}
- [17] LHCb collaboration, LHCb reoptimized detector design and performance: Technical Design Report, CERN-LHCC-2003-030. LHCb-TDR-009
- [18] LHCb collaboration, Performance of the LHCb Vertex Locator, [arXiv:1405.7808v2](https://arxiv.org/abs/1405.7808v2) (2014)
- [19] LHCb collaboration, The LHCb Detector at the LHC, DOI 10.1088/1748-0221/3/08/S08005 (2008)
- [20] Hermann Kolanoski, Norbert Wermes, Teilchendetektoren, Grundlagen und Anwendungen, Heidelberg, Springer Spektrum, 2016, <https://doi.org/10.1007/978-3-662-45350-6>

- [21] M. Adinolfi et al., Performance of the LHCb RICH detector at the LHC, *Eur. Phys. J. C* 73 (2013) 2431, [arXiv:1211.6759](https://arxiv.org/abs/1211.6759)
- [22] LHCb collaboration, LHCb Detector Performance, *Int. J. Mod. Phys. A* 30,1530022 (2015), [arXiv:1412.6352v2](https://arxiv.org/abs/1412.6352v2)
- [23] “CERN - The LHCb collaboration” [LHCb Trigger Scheme \(cern.ch\)](https://cern.ch)
- [24] Barbara Sciascia, LHCb Run 2 Trigger Performance, LHCb-PROC-2016-020
- [25] Maria Grazia Pia, Georg Wiedenspointer, Monte Carlo Simulation for particle Detectors, 06.2012, [arXiv:1208.0047](https://arxiv.org/abs/1208.0047)
- [26] [LHCb Performance Numbers \(cern.ch\)](https://cern.ch), LHCb speakers bureau
- [27] V. Gligorov , Triggering in high energy physics experiments, 13.07.2012, Petnica
- [28] J. Albrecht, The LHCb Trigger System
- [29] LHCb collaboration, Measurement of B^+ , B^0 , B_s^0 and Λ_b^0 production asymmetries in 7 and 8 TeV proton-proton collisions, [arXiv:1703.08464v2](https://arxiv.org/abs/1703.08464v2) (2017)
- [30] LHCb collaboration, Measurement of the D^\pm production asymmetry in 7 TeV pp collisions, <https://doi.org/10.1016/j.physletb.2012.11.038> (2013)
- [31] LHCb collaboration, Measurement of D_s^\pm production asymmetry in pp collisions at $\sqrt{s} = 7$ and 8 TeV, CERN-EP-2018-073 (2018)
- [32] A. Hoecker et al. TMVA-Toolkit for Multivariate Data Analysis, [arXiv:physics/0703039](https://arxiv.org/abs/physics/0703039)
- [33] Kolmogorov–Smirnov Test. In: *The Concise Encyclopedia of Statistics*. Springer, New York, NY. (2008) https://doi.org/10.1007/978-0-387-32833-1_214
- [34] Simone Stracka, John Walsh, Measurement of direct CP asymmetries in $D_{(s)}^+ \rightarrow \eta^{(\prime)} \pi^+$ decays with Run2 data, 27.04.2022, LHCb-ANA_2021_028
- [35] Monte Carlo Particle Numbering Scheme, Revised August 2019 by F. Krauss (Durham U.), S. Navas (Dp.de Fisica. U. de Granada), P. Richardson (Durham U.) and T. Sjöstrand (Lund U.)
- [36] G. Cowan, Topics in statistical data analysis for high energy physics, [arXiv:1012.3589](https://arxiv.org/abs/1012.3589) (2010)
- [37] Johnson, N. L. “Systems of Frequency Curves Generated by Methods of Translation.” *Biometrika*, vol. 36, no. 1/2, 1949, pp. 149–76. *JSTOR*, <https://doi.org/10.2307/2332539>. Accessed 28 July 2023.
- [38] Rene Brun and Fons Rademakers, ROOT - An Object Oriented Data Analysis Framework, Proceedings AIHENP'96 Workshop, Lausanne, Sep. 1996, *Nucl. Inst. & Meth. in Phys. Res. A* 389 (1997) 81-86. See also "ROOT" [software], Release v6.28/02, 23/03/2023
- [39] N. Karjanto, Properties of Chebyshev polynomials, [arXiv:2002.01342v1](https://arxiv.org/abs/2002.01342v1) (2002)

Acknowledgement

I want to express my gratitude for Prof. Hansmann-Menzemer for the opportunity to write my bachelor thesis in her group. Many thanks to Dr. Giulia Tuci for the nice introduction to this research field and the continuous support through some problems. Thanks to the rest of the LHCb group in Heidelberg for their warm welcome. Special thanks to my office mates for the interesting discussions and the friendly atmosphere.

Erklärung

Ich versichere, dass ich diese Arbeit selbstständig verfasst und keine anderen als die angegebenen Quellen und Hilfsmittel benutzt habe.

Heidelberg, den 04.10.2023,

A handwritten signature in blue ink, consisting of a stylized first name followed by a surname, all enclosed within a large, sweeping loop.